UCLA
UCLA Previously Published Works

Title
Imaging Dielectric Breakdown in Valence Change Memory

Permalink
https://escholarship.org/uc/item/37z5f5vv

Journal
Advanced Functional Materials, 32(2)

ISSN
1616-301X

Authors
Hubbard, William A
Lodico, Jared J
Chan, Ho Leung
et al.

Publication Date
2022

DOI
10.1002/adfm.202102313

Copyright Information
This work is made available under the terms of a Creative Commons Attribution License, availalbe at https://creativecommons.org/licenses/by/4.0/

Peer reviewed

eScholarship.org Powered by the California Digital Library
University of California

Imaging Dielectric Breakdown in Valence Change Memory

William A. Hubbard,[1,2,†] *Jared J. Lodico,*[1,2,†] *Ho Leung Chan,*[1,2]
Matthew Mecklenburg,[3] *B.C. Regan*[1,2,*]

[1]Department of Physics and Astronomy, University of California, Los Angeles, CA 90095, U.S.A.
[2]California NanoSystems Institute, University of California, Los Angeles, CA 90095, U.S.A.
[3]Core Center of Excellence in Nano Imaging, University of Southern California, Los Angeles, CA 90089, U.S.A.
[*]To whom correspondence should be addressed; E-mail: regan@physics.ucla.edu

Keywords: *RRAM, dielectric breakdown, hafnium oxide, STEM EBIC, device physics*

Dielectric breakdown (DB) controls the failure, and increasingly the function, of microelectronic devices. Standard imaging techniques, which generate contrast based on physical structure, struggle to visualize this electronic process. Here we report *in situ* scanning transmission electron microscopy (STEM) electron beam-induced current (EBIC) imaging of DB in Pt/HfO_2/Ti valence change memory devices. STEM EBIC imaging directly visualizes the electronic signatures of DB, namely local changes in the conductivity and in the electric field, with high spatial resolution and good contrast. We see DB proceeding through two distinct structures arranged in series: a volatile, "soft" filament created by electron injection; and a non-volatile, "hard" filament created by oxygen-vacancy aggregation. This picture makes a physical distinction between "soft" and "hard" DB, while at the same time accommodating "progressive" DB, where the relative lengths of the hard and soft filaments can change on a continuum.

Introduction

Dielectric films, generally oxides, are key elements in all microelectronic devices (*1, 2*). The basic computing unit of the modern, information-based economy, the transistor, contains a dielectric film at its heart, as does the simple capacitor. Such films are also the switching component in the resistive random access memory (RRAM) elements that might soon constitute much of fast digital storage (*2–4*) and neuromorphic processors (*3, 5*). Depending on the application, conduction in nominally insulating dielectric films can be central to device function (RRAM) or failure (gate dielectrics, capacitors). The reliability of computing hardware, present and future, thus depends critically on the detailed mechanisms underlying controlled and uncontrolled dielectric breakdown (DB) in these insulators.

Because RRAM devices feature controlled DB (*2, 6–9*) that can be switched ON and OFF repeatedly, they represent an ideal target for a study of DB. For oxide-based RRAM (known as valence change memory — VCM— or OxRAM) in particular, many details about the switching process are poorly understood. Unsettled issues involve the filament growth direction (toward the cathode (*4, 10–12*) or away from it (*13, 14*)), the filament conduction method (*15*), and the filament morphology (*8, 15*). Incomplete understanding of the physics and chemistry that drive switching in VCM is the main obstacle to its optimization and commercialization (*3, 15, 16*).

Direct imaging of DB in VCM has the potential to reveal critical details about the switching mechanisms, but visualizing a dynamic and fundamentally electronic process occurring inside a bulk solid is extremely challenging (*5*). DB has been imaged using SPM (*17–21*),

SEM (*22–24*), X-rays (*25, 26*), and TEM (*12, 14, 20, 22, 27–31*). Standard SPM, SEM, X-ray, and TEM imaging are sensitive to physical structure: the arrangement of atoms (*22, 24, 27*), and perhaps their chemical identities (*12, 20, 25–30, 32*). But the changes to the physical structure of an insulator can be *millions* of times smaller — and thus more difficult to visualize — than the changes to its electronic structure. For example, doping at a level of 10^{-5} can change the conductivity by a factor of 10^3 (*33*). Thus standard imaging techniques show DB in the limit where marked changes to the physical structure occur, such as bubbling (*17, 18, 22, 24*), clustering (*20, 29, 32*), and crystallization (*20, 22–24, 27, 31*). This physically-stressed limit is not necessarily the regime of interest, especially in the case of RRAM, where the DB must be controlled and reversible (*24, 27*).

Electronic signatures of DB can be visualized with modified versions of the standard imaging techniques. Conductive atomic force microscopy (CAFM) (*8, 20*), scalpel scanning probe microscopy (*19*), scanning tunneling microscopy (*21*), *in situ* TEM holography (*14*), and electron beam-induced current imaging (EBIC) in an SEM (*23*) have been used to image changes to the local conductivity and electric fields associated with DB. However, these imaging technique struggle with poor perspective (spatial or temporal), imaging artifacts, and/or low contrast (*5*). To date it has not been possible to perform high-contrast imaging of cycling in a clean VCM device at nm-scale resolution.

To address these issues we fabricate Pt/HfO_2/Ti VCM devices in a slant-vertical architecture (Fig. 1) and then image them using STEM EBIC. Since its implementation as a high-κ gate dielectric in 2007, HfO_2 (hafnia) has been considered perhaps *the* preferred dielectric for transistor, flash memory, and RRAM applications (*7, 16*). The slant-vertical architecture maintains a realistic RRAM device topology while simultaneously allowing good TEM imaging access. This architecture has previously revealed the movement of Cu atoms (atomic number $Z = 29$) in Cu/Al_2O_3 conductive bridge memory (CBRAM) over multiple switching cycles (*34*). However, the oxygen atom ($Z = 8$), or, more precisely, vacancy movement thought to mediate VCM switching (*6, 7, 9, 15*) is too subtle to be detected in an Hf ($Z = 72$) background with standard TEM imaging. We therefore also image the slant-vertical VCM devices using STEM electron beam-induced current (EBIC) imaging. STEM EBIC imaging has two important contrast modes: the standard mode, which generates its contrast based on electron-hole pair separation (*35, 36*), and a recently-developed mode that generates contrast via the emission of secondary electrons (SEEBIC) (*37*). Because standard EBIC and SEEBIC imaging are sensitive to local electric fields (*35, 36*) and to the local conductivity (*37, 38*), respectively, these imaging modalities are uniquely suited for mapping the effects of DB at high spatial resolution (*39*).

Results and Discussion

As detailed below, we observe DB proceeding in two steps. Increasing the Ti–Pt bias voltage from zero first produces a volatile, or "soft", filament. This structure, which we attribute to charge injection into existing oxygen vacancies, vanishes when the bias voltage is removed. Further increasing the bias voltage eventually produces a non-volatile, or "hard", filament.

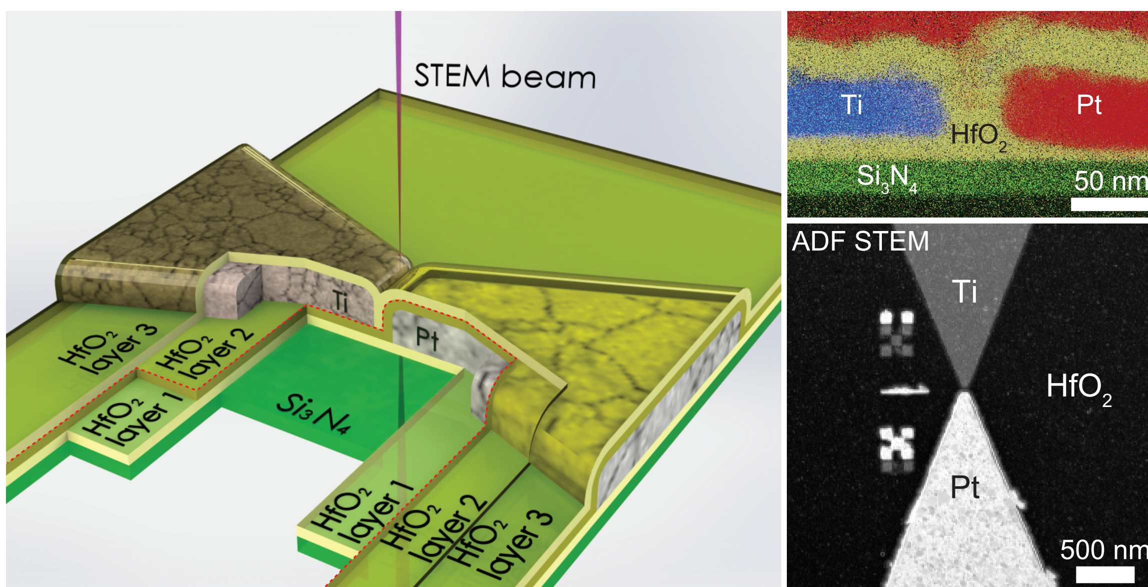

Figure 1: **VCM slant-vertical device architecture.** (left) A VCM device, shown entirely to-scale with cutaways, consists of ALD HfO_2, a Pt electrode, ALD HfO_2, a Ti electrode, and a capping layer of ALD HfO_2, deposited in this order on a Si_3N_4 support membrane. As highlighted by the red dotted line, sequential layer deposition ensures that, regardless of the horizontal gap, the electrodes are always separated by the second (conformal) layer of HfO_2. (right top) X-ray energy dispersive spectroscopy (EDS) data from a FIB-prepared cross section of a slant-vertical device show its elemental composition (see also Figs. S1–S2). None of our switching experiments use this point-of-view. (right bottom) Low magnification ADF STEM shows a slant-vertical device in plan-view, the perspective adopted for all switching experiments.

The hard filament, which we attribute to the production and aggregation of new oxygen vacancies, remains if the bias voltage is set to 0 V, but it can be dissolved by reversing the voltage bias. The hard filament conducts ohmically, while the soft filament conducts via the Poole-Frenkel mechanism. A complete filament puts the VCM device in the ON state and consists of distinct hard and soft filaments arranged in series, with the latter limiting the net electrical transport via PF conduction. These filaments can be associated with regions of hard and soft DB (*40*), respectively.

A slant-vertical Pt/HfO_2/Ti VCM device (Fig. 1) imaged in plan-view affords a side-on perspective of the switching region (*34*). The top (Ti) and bottom (Pt) electrodes are both completely encased in HfO_2, with a continuous HfO_2 layer separating them (see Methods). This architecture avoids the focused ion beam (FIB) sample preparation (*12, 14, 22, 28, 29, 32*) often used to create cross-sectional TEM samples, which introduces additional, compromising interfaces, structural damage, and chemical (e.g. gallium) contamination that have the potential to alter the DB process under study (*5*). Thus we have good STEM imaging access in clean, microfabricated devices with a realistic (i.e. vertically stacked) topology.

We cycle a device up to a potential just below the switching potential and then back to zero (Fig. 2, Movie S1). While the bias current is initially small, it is easily measured and increases exponentially, from 5 pA at 1 V, to 20 pA at 20 V, in this device (see also Fig. 4). Annular dark field (ADF) STEM imaging of the device essentially maps the proton column density — the Pt ($Z = 78$) electrode generates more signal than the Ti ($Z = 22$) electrode (Fig. 2, top row). (The Si_3N_4 and HfO_2 are very and mostly uniformly distributed, respectively, across this field of view.) Unsurprisingly, standard STEM ADF imaging of the device shows no changes as the device begins to conduct. Although cation motion has been observed in valence change chemistries (*21*), the absence of ADF contrast changes like those seen in Ref. 34 with a similar device architecture indicates that few, if any, of the heavy nuclei in the sample are relocating as a result of the applied potential.

STEM EBIC imaging (Fig. 2, second row), on the other hand, reveals the VCM device's changing conductivity and connectivity landscape (*37*). In the device's OFF state the Pt electrode is well-isolated from the Ti and thus is only connected to the transimpedance amplifier (TIA) that measures the EBIC. When the beam is incident on the Pt, secondary electrons (SEs) are ejected from the sample, the holes left behind reach the TIA, and this positive current gives bright contrast. When the beam is incident on the Ti, SEs are also ejected, but the corresponding holes go to ground through the Ti. While the TIA does not register these holes, a portion of the emitted SEs are recaptured (*37*) in the Pt and the resulting negative current in the Pt produces dark contrast. When the beam is not incident on an electrode, few SEs are produced and the contrast resulting is a neutral gray.

Even subtle, pre-switching electronic changes are immediately visible with STEM EBIC imaging. (Fig. 2, second row). With no applied bias the Pt electrode has the same shape whether viewed with ADF or with EBIC, but as the bias is increased, the Pt electrode, viewed with EBIC, swells. With a 10 V bias, a bright region grows from the Pt edge towards the Ti. With 17.5 V applied, this bright region grows even closer to the Ti electrode, with an especially bright feature appearing at the apex of the protrusion slightly to the right of frame center. When

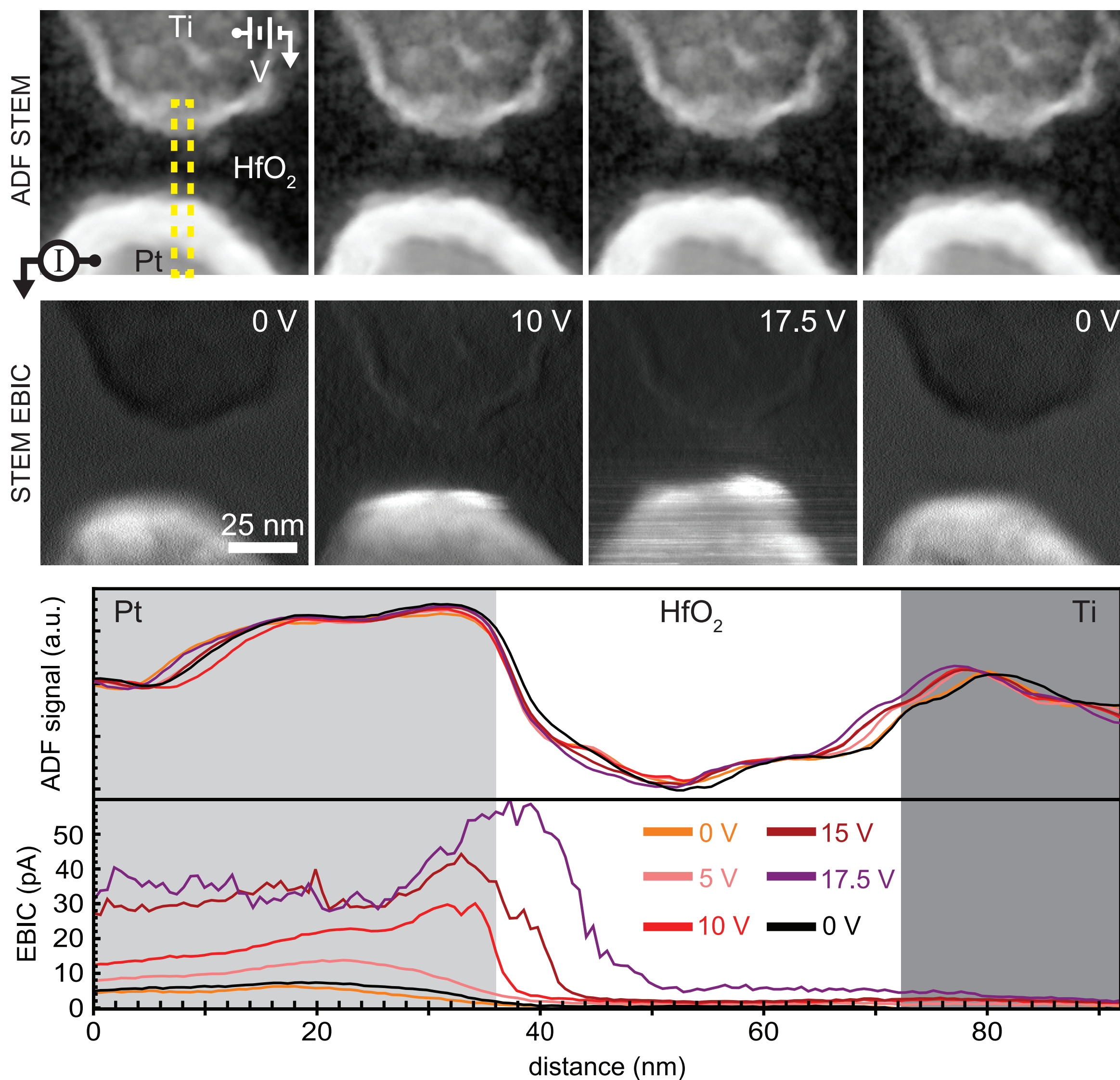

Figure 2: **Soft filament formation and dissolution.** (top row) STEM ADF images of a slant-vertical Pt/HfO_2/Ti VCM device show no changes as the Ti–Pt bias voltage is increased. (second row) Simultaneously acquired STEM EBIC images, on the other hand, show the region electrically connected to the Pt expanding into the gap. See also Movie S1. (bottom) Line profiles extracted by averaging over the rectangular region indicated in the first ADF image show these trends quantitatively (including additional bias values from images not shown). Symbols in the first ADF image indicate the electrical connections for applying the bias and measuring the EBIC.

the bias is removed, the bright structure disappears and the electrode, as viewed with STEM EBIC, reverts to its initial configuration. This structure is thus both conducting and volatile.

Line profiles (Fig. 2, bottom) extracted from these images and others not shown present these results more quantitatively. The ADF data (both images and line profiles) show no contrast changes as a function of increasing bias, other than some small shifts attributable to sample drift over the 90 s image-acquisition period. The corresponding EBIC data, however, show a conducting region that extends farther and farther into the gap, reaching almost halfway across at the final high bias of 17.5 V before disappearing entirely when the bias is returned to 0 V.

These volatile conducting structures ("soft" filaments) that form prior to switching (see also Figs. 3, S3, and S7 and Movies S1–5) appear under both Ti-Pt bias polarities and always grow from the cathode to anode (low to high potential), as expected for electron-charge injection. With the Pt held at virtual ground, for example, a soft filament grows from the Pt under positive Ti bias and from the Ti under negative Ti bias (Fig. S7).

In the STEM EBIC images discussed above, the contrast is dominated by SEEBIC, which is generated by secondary electron emission. Standard EBIC contrast, on the other hand, is generated by the separation of electron-hole pairs in a local electric field E. As the soft filament extends across the gap, the local E-field increases like V/d, where V is the applied potential and d is the width of the remaining gap (Fig. 3). At low potentials, SEEBIC dominates the contrast and shows the soft filament extending from the cathode (e.g. Fig 2 and first two columns of Fig. 3). At high potentials the device is ON and cannot be EBIC-imaged under bias because the much-larger device current swamps the EBIC. However, in a very narrow, intermediate potential range, the E-field is large enough to separate electron-hole pairs, and yet not so large that device conduction saturates the TIA (Fig. 3, third column). Here standard EBIC contrast dominates the SEEBIC contrast (see Figs. S4–S5), vividly highlighting the large E-field in the region extending from the tip of the soft filament to the Ti electrode. (See also Figs. S6, S7, S9, and Movies S2–S5.) Line profiles show that the peak EBIC, and thus the peak E-field, is in fact at the Ti interface (Fig. 3, bottom). Up to this point in the switching cycle, the observed changes are all volatile, in that returning the applied bias to 0 V causes the filamentary structures observed to disappear (Fig. 3, fourth column).

Applying just over 20 V bias to the Ti electrode of the Fig. 2 device causes it to transition from the high-resistance state (HRS) (rightmost Fig. 2 = leftmost Fig. 4) to the low-resistance state (LRS) (Fig. 4 middle). The device current accordingly jumps to the pre-programmed current limit of 50 nA (Fig. 4 plot) (*34*). Continuing the STEM EBIC image series of Fig. 2 then becomes impossible because at high bias the ON-state device current saturates the TIA. Therefore we reduce the device bias voltage to zero for imaging.

While (again) no changes are seen with ADF, even without the applied bias STEM EBIC reveals that the transition to the LRS is accompanied by a change in the HfO_2: a new, conducting region electrically connected to the Pt electrode now extends into the gap. Since it appears at 0 V, by definition this change is non-volatile, or "hard", and it appears where the soft filament generates its most intense SEEBIC signal (Fig. 2). The hard filament does not bridge the entire gap between electrodes (see also Figs. S8, S10, S11, and S14).

After a -10 V RESET, the device returns to the HRS and the hard filament is almost en-

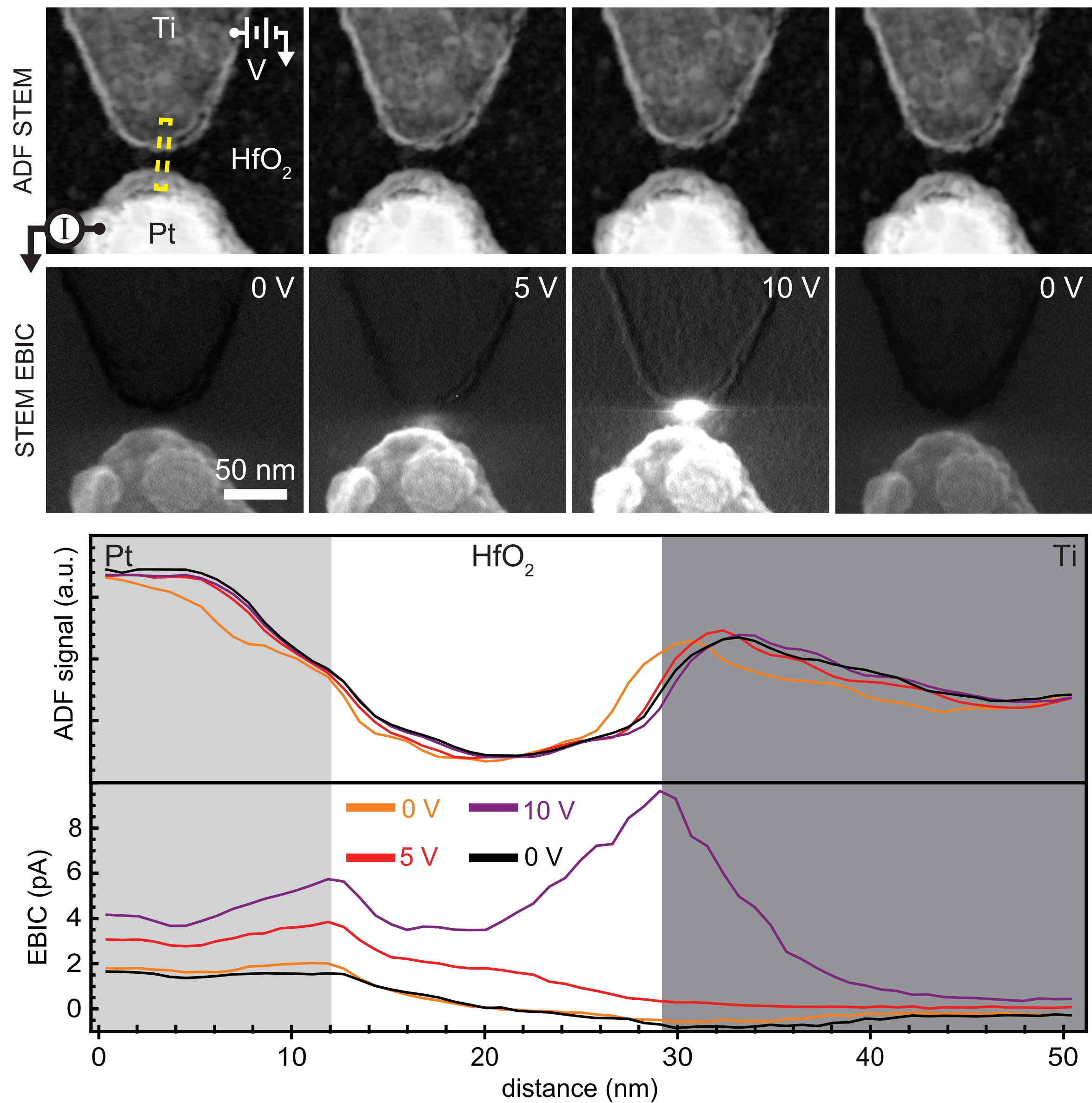

Figure 3: **Large E-field at the switching point.** (top) STEM ADF imaging shows no changes as a Ti/HfO_2/Pt device is biased at 0 V, 5 V, and 10 V, and 0 V. (second row) EBIC imaging shows a soft filament grow, almost connect, and then disappear. See also Movie S3. (bottom) Line profiles of the ADF and EBIC signals from the dashed yellow region indicated in the 0 V ADF image show the corresponding contrast values quantitatively. At non-zero bias, small device currents (e.g. 300 fA at 10 V) add to the EBIC (Fig. S6).

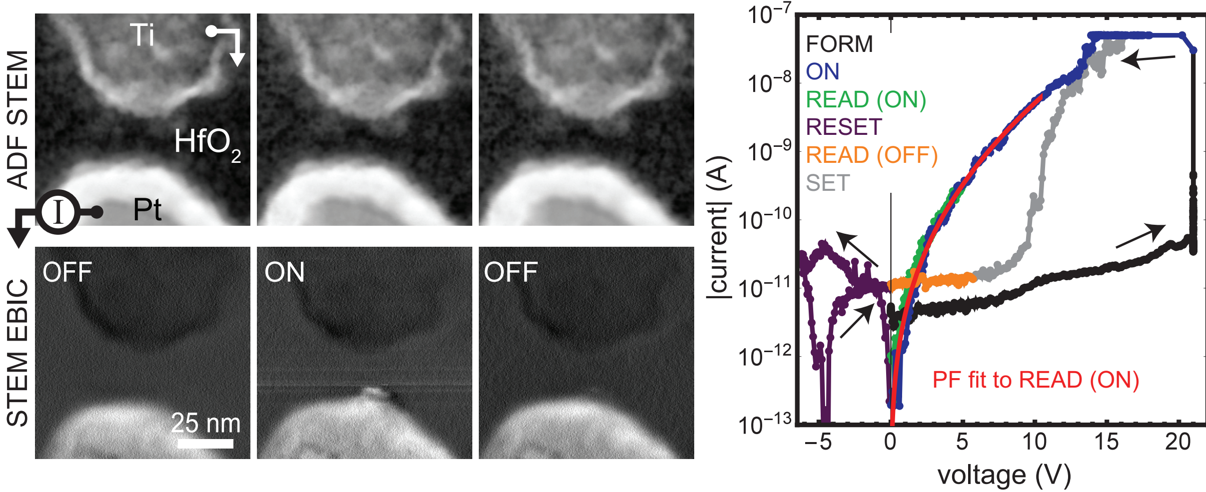

Figure 4: **Hard filament formation and dissolution.** ADF imaging (left, top row) shows no changes between the ON and OFF states of the VCM device of Fig. 2. STEM EBIC imaging (left, bottom row), however, again shows obvious changes between the ON and OFF states, with the most marked being a sharp protuberance at the Pt electrode's apex. Each image is acquired after voltage programming (see text), but with a 0 V bias. The $I - V$ plot (right) shows a complete cycle of this device. The LRS data is well fit by the PF model (red curve). The apparent "battery" (i.e. current $I \neq 0$ at voltage $V = 0$ and vice versa) in the HRS is an artifact of stray capacitance, the large device resistance, and the voltage ramp rate $dV/dt = 0.3$ V/s. Note that, because of device currents and beam sensitivity, STEM EBIC images cannot be directly associated with all points on the plot.

tirely dissolved (Fig. 4 rightmost images). During subsequent cycles the hard filament reappears in the same region in the ON state and disappears (though perhaps incompletely) in the OFF state (Fig. S8).

The current-voltage ($I-V$) plot (Fig. 4) shows a typical FORM/ON/READ/OFF/READ/SET cycle for this device. In the LRS, the transport is well-fit (see SI) by the Poole-Frenkel (PF) conduction model (*9, 41, 42*). Evidence of PF conduction also appears when we image an ON-state device with STEM EBIC while floating the Ti electrode. We image a device after a RESET, after a SET, and again immediately afterward (Fig. 5). For all three images the device is under no applied bias and the Pt electrode is connected to the TIA. The Ti electrode is grounded when the device is nominally OFF (Fig. 5, left column) and floating when nominally ON (Fig. 5, center and right columns). After the RESET (SET) the Ti electrode is dark (bright) in the EBIC image, indicating that the Ti is not (is) connected to the Pt. However, the contrast on the floating Ti electrode, and *only* on the Ti electrode, is streaky when the device is ON (see also Figs. S10 and S11).

The streaking in the Ti is indicative of the device's nonlinear $I - V$ relationship. As the beam rasters across the floating Ti electrode, pixel-by-pixel from left to right and line-by-line from top to bottom, SE ejection causes the Ti to charge positively. Eventually the charging produces a potential sufficient for PF conduction, and the Ti electrode then discharges into the Pt to produce positive (bright) EBIC. Immediately after a discharge the EBIC returns to

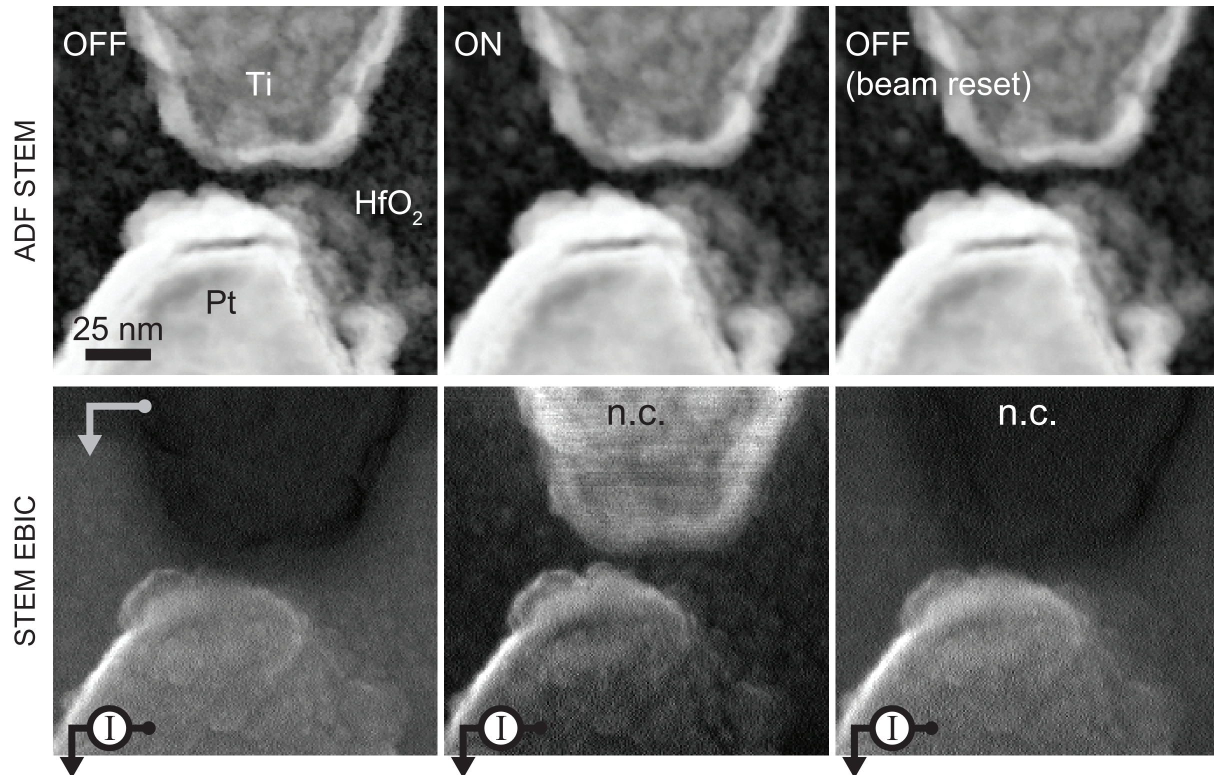

Figure 5: **ON-state conduction switched OFF by STEM beam.** Images acquired directly after a −10 V device RESET (left column) show negative EBIC from the Ti electrode, indicating that the device is OFF. With the beam blanked, the device is then SET and held at 9 V until immediately before another image acquisition (center column). The intermittent positive EBIC from the Ti electrode in this state indicates a non-ohmic connection to the Pt electrode. A final image (right column) immediately following shows only negative EBIC from the Ti electrode, indicating that the device has been RESET by the beam. ADF imaging (top row) shows no sign of these state changes, which are only made evident with EBIC imaging (bottom row). A 'n.c.' label on the Ti electrode indicates 'no external connection'.

a smaller value (gray). This charge/discharge cycle continues across the entire Ti electrode. Imaging with the frame rotated 180° (i.e. starting the raster on the Pt instead of the Ti) does not produce similar streaks on the Pt, which is directly connected to the TIA. (With the rotated scan direction the Ti appears dark for reasons to be discussed shortly.) While a hard filament is visible in this device (see also Fig. S11), this intermittent conduction is not consistent with an ohmic connection between electrodes. The voltage-dependent conduction is indicative of soft breakdown: this device is conducting through a PF soft filament in series with the ohmic hard filament during the first half of the ON-state images (Fig. 5, second column).

To a degree not seen in Cu/Al_2O_3 CBRAM elements (*34*), the VCM devices are beam sensitive, which suggests that this VCM chemistry may be unsuitable for radiation-hard applications and also provides clues as to the mechanisms underlying the ON state conduction. As the beam rasters through the gap (Fig. 5, second column), SE emission produces holes that annihilate the injected electrons constituting the soft filament. As a result, images acquired immediately afterward (Fig. 5, third column) and subsequent transport measurements show the device to be OFF. We find that electron beam exposure steadily increases the device resistance, eventually switching an ON device OFF (Fig. S13). Even a few seconds of exposure, as occurs while pre-viewing the field of view prior to the longer EBIC image acquisition, typically returns a device in the LRS to the HRS. The change is especially rapid when the beam is imaging the region between the electrodes (Fig. S12). Transport in the beam-induced HRS more closely resembles the higher-resistance pre-forming state than the voltage-induced (i.e. deliberate RESET) HRS. The device can then be "re-formed" into the ON state and will subsequently cycle normally.

Hard filaments are relatively robust to repeated EBIC image acquisition (Fig. S14). While an $I - V$ shows that imaging an ON device switches it OFF, a second EBIC image shows the hard filament to be almost unchanged. The sensitivity of the device conductance to the beam, combined with the relative insensitivity of the hard filament to the beam, suggests that the beam primarily affects the soft portion of the ON-state filament. Imaging the filament with an electron beam ejects SE, leaving holes behind that annihilate trapped electrons (*16*) and destroy the soft filament, which RESETs the device. Devices which receive a large electron dose eventually fail into a persistent LRS; the Figs. 2, 4 device switched reliably over dozens of cycles, failing after 40 EBIC images, each of which represents a dose of 3×10^6 e/nm^2.

We understand our observations in terms of the following model (Fig. 6). In a pristine device, the low density of oxygen vacancies in the ALD-deposited HfO_2 does not support electrical conduction between the Pt bottom electrode and the Ti top electrode (*43*). The oxygen vacancies are present in a variety of charge states and aggregation numbers (*44, 45*). Applying a positive voltage bias to the top electrode injects electrons from the bottom electrode into nearby pre-existing vacancies (*42,46*). These vacancies PF-conduct and constitute the soft filament, which grows (Fig. 2) from the cathode (here the bottom electrode) independent the electrode materials. With sufficient positive voltage bias, the soft filament eventually approaches the top electrode, producing a large electric field across the remaining gap (Fig. 3). In this field some Ti is oxidized, creating new, positively-charged oxygen vacancies (*8, 15, 26, 44*). These positively-charged vacancies are especially mobile in the HfO_2 and are likely doubly-

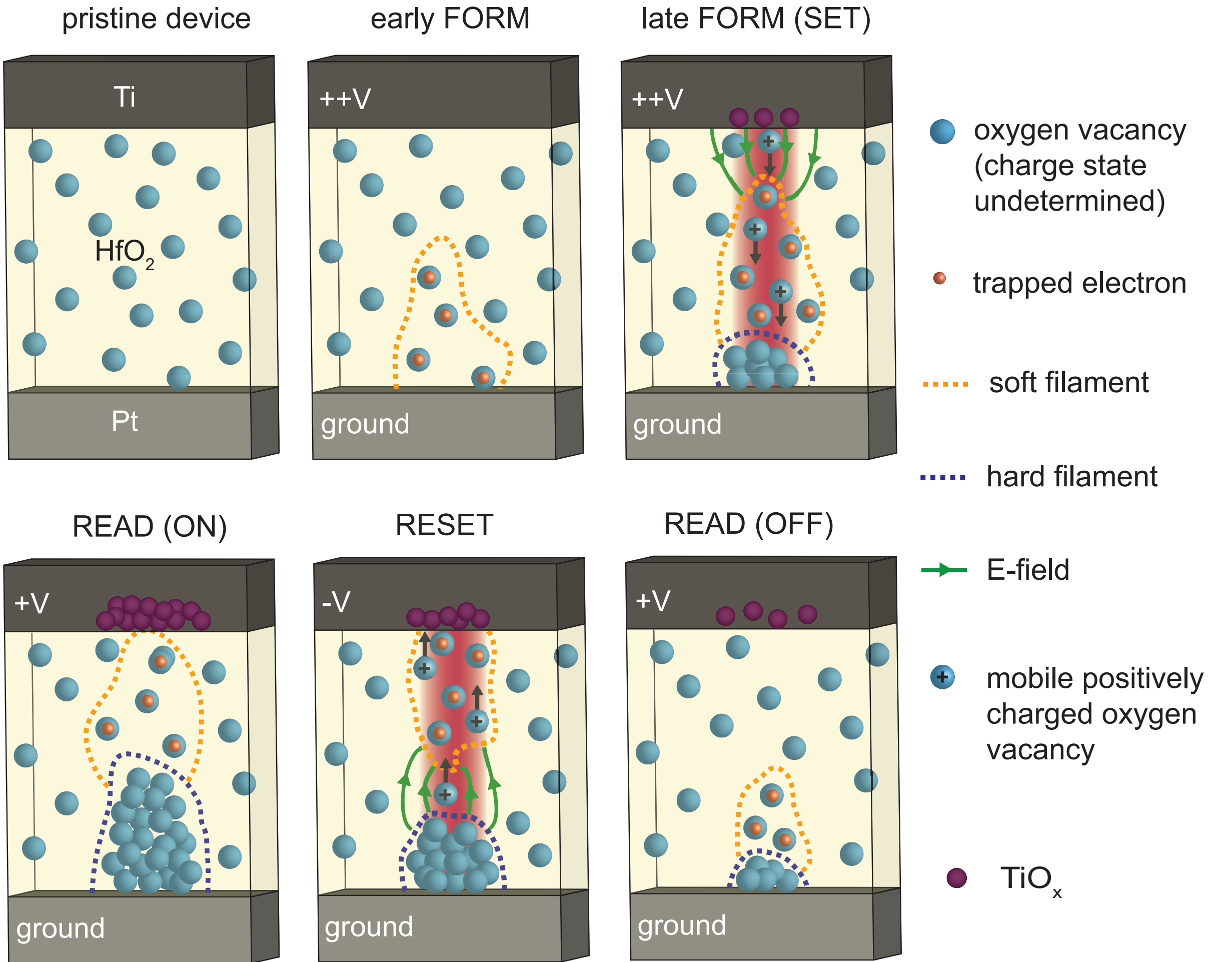

Figure 6: **Model of the HfO_2 VCM switching process (*43*).** In Pt/HfO_2/Ti devices both hard and soft filaments are observed to grow from the bottom (Pt) electrode (cathode) toward the top (Ti) electrode (anode) during a SET (*13, 14*). STEM EBIC imaging visualizes all of this switching process's key features: the soft filament (Fig. 2), the hard filament (Fig. 4), the strong electric fields immediately preceding SET (Fig. 3), and the charge-sensitive conduction mechanism (Fig. 5).

charged (*8, 44, 45*). They drift in the E-field through the dielectric until they establish ohmic contact with the bottom electrode, where they are reduced. In sufficient concentration these oxygen vacancies dope the HfO_2 into ohmic conduction (*15, 26*) and constitute the hard filament, which, like the soft filament, also grows up from the bottom electrode (Fig. 4). This conducting filament growth resulting from positively-charged vacancies moving from the anode to the cathode is directly analogous to that seen with metal cations in CBRAM (*15, 34*). The cathode-to-anode growth direction indicates that the oxygen exchange rate at the Ti is slow compared to the vacancy migration through the HfO_2 (*15*). The vacancy transport and PF conduction currents generate Joule heating, which accelerates the transport and reaction rates and leads to positive feedback (*8, 15*). The creation of the hard filament, which generally does not span the entire gap between the electrodes, completes the forming process. With a current limit, as in VCM, the hard filament growth is regulated and the DB is controlled. With a voltage limit, as in a transistor or capacitor, positive feedback can produce uncontrolled, runaway DB and a catastrophic failure.

With hard and soft filaments in series, a small positive potential can drive an electrical current and the VCM device is in the ON state (Figs. 4–5). Zeroing the applied bias causes the soft filament to retract from the top electrode as electrons return to the bottom electrode. Reversing the applied bias injects electrons from the other side, causing a soft filament to grow from the top electrode towards the bottom. Larger negative bias oxidizes the hard filament starting at its tip (*8*), producing a RESET. Post-forming SET occurs at a lower voltage than the initial FORM (Fig. 4) because of both trapped charge and the remaining hard filament.

This picture of DB in VCM makes a physical distinction between hard and soft breakdown, which historically have been difficult to distinguish (*2*): the former involves the motion of atoms, ions, or vacancies, while the latter involves the motion of electrons or holes. As the motion of electrons is more easily reversed, to achieve the controllable, reversible DB required for memory function, at least part of the conducting filament in VCM should be soft. Thus the ideal VCM ON-state represents an intermediate condition between the soft and hard breakdown limits; larger currents lead to harder breakdown, with thermal runaway and an unswitchable VCM device at the endpoint (*24*). This DB picture moreover provides a clear theoretical framework that offers specific directives on how to optimize VCM switching parameters such as speed, retention, and longevity. During device fabrication the oxide density and its doping, for instance, might be independently tuned to separately address the ionic transport and electronic conduction, respectively, allowing direct control of the critical hard/soft filament length ratio. This model of DB is broadly consistent with previous findings, not only in HfO_2 (*13, 14, 17*), but also in other binary oxides such as TiO_2 and Ta_2O_5 (*18, 47–49*).

Within the broader field of DB generally, these results provide a framework for understanding the distinction, or lack thereof, between hard and soft breakdown on the one hand, and (possibly time-dependent) progressive breakdown on the other (*2, 3, 8, 50*). With high-contrast, high-resolution imaging, hard and soft breakdown are physically distinguishable as described here, but without such imaging DB appears to occur on a progressive continuum, where the progression is measured by the unseen relative lengths of hard and soft filaments arranged in series.

References

1. Wallace, R. M. Dielectric Materials for Microelectronics. In Kasap, S. & Capper, P. (eds.) *Springer Handbook of Electronic and Photonic Materials*, Springer Handbooks, 615–644 (Springer International Publishing, Cham, 2017).

2. Palumbo, F., Wen, C., Lombardo, S., Pazos, S., Aguirre, F., Eizenberg, M., Hui, F. & Lanza, M. A Review on Dielectric Breakdown in Thin Dielectrics: Silicon Dioxide, High-*k* , and Layered Dielectrics. *Advanced Functional Materials* 1900657 (2019).

3. International Roadmap for Devices and Systems. Tech. Rep. 2020, IEEE (2020). https://irds.ieee.org/.

4. Padovani, A., Larcher, L., Padovani, P., Cagli, C. & Salvo, B. D. Understanding the Role of the Ti Metal Electrode on the Forming of HfO_2-Based RRAMs. In *2012 4th IEEE International Memory Workshop*, 1–4 (2012).

5. Lanza, M. *et al.* Recommended Methods to Study Resistive Switching Devices. *Advanced Electronic Materials* **0**, 1800143 (2019).

6. Fang, Z., Yu, H. Y., Liu, W. J., Wang, Z. R., Tran, X. A., Gao, B. & Kang, J. F. Temperature Instability of Resistive Switching on HfO_x-Based RRAM Devices. *IEEE Electron Device Letters* **31**, 476–478 (2010).

7. Gonon, P., Mougenot, M., Vallée, C., Jorel, C., Jousseaume, V., Grampeix, H. & El Kamel, F. Resistance switching in HfO_2 metal-insulator-metal devices. *Journal of Applied Physics* **107**, 074507 (2010).

8. Bersuker, G., Gilmer, D. C., Veksler, D., Kirsch, P., Vandelli, L., Padovani, A., Larcher, L., McKenna, K., Shluger, A., Iglesias, V., Porti, M. & Nafría, M. Metal oxide resistive memory switching mechanism based on conductive filament properties. *Journal of Applied Physics* **110**, 124518 (2011).

9. Walczyk, C., Walczyk, D., Schroeder, T., Bertaud, T., Sowinska, M., Lukosius, M., Fraschke, M., Wolansky, D., Tillack, B., Miranda, E. & Wenger, C. Impact of Temperature on the Resistive Switching Behavior of Embedded HfO_2-Based RRAM Devices. *IEEE Transactions on Electron Devices* **58**, 3124–3131 (2011).

10. Lin, Y. S., Zeng, F., Tang, S. G., Liu, H. Y., Chen, C., Gao, S., Wang, Y. G. & Pan, F. Resistive switching mechanisms relating to oxygen vacancies migration in both interfaces in Ti/HfOx/Pt memory devices. *Journal of Applied Physics* **113**, 064510 (2013).

11. Sokolov, A. S., Jeon, Y.-R., Kim, S., Ku, B., Lim, D., Han, H., Chae, M. G., Lee, J., Ha, B. G. & Choi, C. Influence of oxygen vacancies in ALD HfO_{2-x} thin films on non-volatile resistive switching phenomena with a Ti/HfO2-x/Pt structure. *Applied Surface Science* **434**, 822–830 (2018).

12. Yang, Y., Lü, W., Yao, Y., Sun, J., Gu, C., Gu, L., Wang, Y., Duan, X. & Yu, R. In situ TEM Observation of Resistance Switching in Titanate Based Device. *Scientific Reports* **4**, 3890 (2014). Number: 1 Publisher: Nature Publishing Group.

13. Hudec, B., Wang, I.-T., Lai, W.-L., Chang, C.-C., Jančovič, P., Fröhlich, K., Mičušík, M., Omastová, M. & Hou, T.-H. Interface engineered HfO_2-based 3d vertical ReRAM. *Journal of Physics D: Applied Physics* **49**, 215102 (2016).

14. Li, C., Gao, B., Yao, Y., Guan, X., Shen, X., Wang, Y., Huang, P., Liu, L., Liu, X., Li, J., Gu, C., Kang, J. & Yu, R. Direct Observations of Nanofilament Evolution in Switching Processes in HfO_2-Based Resistive Random Access Memory by In Situ TEM Studies. *Advanced Materials* **29**, 1602976 (2017).

15. Menzel, S. & Waser, R. 4 - Mechanism of memristive switching in OxRAM. In Magyari-Köpe, B. & Nishi, Y. (eds.) *Advances in Non-Volatile Memory and Storage Technology (Second Edition)*, Woodhead Publishing Series in Electronic and Optical Materials, 137–170 (Woodhead Publishing, 2019).

16. Gritsenko, V. A., Perevalov, T. V. & Islamov, D. R. Electronic properties of hafnium oxide: A contribution from defects and traps. *Physics Reports* **613**, 1–20 (2016).

17. Jeong, D. S., Schroeder, H., Breuer, U. & Waser, R. Characteristic electroforming behavior in Pt/TiO_2/Pt resistive switching cells depending on atmosphere. *Journal of Applied Physics* **104**, 123716 (2008). Publisher: American Institute of Physics.

18. Yang, J. J., Miao, F., Pickett, M. D., Ohlberg, D. A. A., Stewart, D. R., Lau, C. N. & Williams, R. S. The mechanism of electroforming of metal oxide memristive switches. *Nanotechnology* **20**, 215201 (2009). Publisher: IOP Publishing.

19. Celano, U., Op de Beeck, J., Clima, S., Luebben, M., Koenraad, P. M., Goux, L., Valov, I. & Vandervorst, W. Direct Probing of the Dielectric Scavenging-Layer Interface in Oxide Filamentary-Based Valence Change Memory. *ACS Applied Materials & Interfaces* **9**, 10820–10824 (2017).

20. Raghavan, N., Pey, K. L. & Shubhakar, K. High-κ dielectric breakdown in nanoscale logic devices – Scientific insight and technology impact. *Microelectronics Reliability* **54**, 847–860 (2014).

21. Wedig, A., Luebben, M., Cho, D.-Y., Moors, M., Skaja, K., Rana, V., Hasegawa, T., Adepalli, K. K., Yildiz, B., Waser, R. & Valov, I. Nanoscale cation motion in TaO_x, HfO_x and TiO_x memristive systems. *Nature Nanotechnology* **11**, 67–74 (2016).

22. Kwon, D.-H., Kim, K. M., Jang, J. H., Jeon, J. M., Lee, M. H., Kim, G. H., Li, X.-S., Park, G.-S., Lee, B., Han, S., Kim, M. & Hwang, C. S. Atomic structure of conducting nanofilaments in TiO_2 resistive switching memory. *Nature Nanotechnology* **5**, 148–153 (2010).

23. Hoskins, B. D., Adam, G. C., Strelcov, E., Zhitenev, N., Kolmakov, A., Strukov, D. B. & McClelland, J. J. Stateful characterization of resistive switching TiO_2 with electron beam induced currents. *Nature Communications* **8** (2017).

24. Meng, J., Zhao, B., Xu, Q., Goodwill, J. M., Bain, J. A. & Skowronski, M. Temperature overshoot as the cause of physical changes in resistive switching devices during electroformation. *Journal of Applied Physics* **127**, 235107 (2020).

25. Kumar, S., Graves, C. E., Strachan, J. P., Grafals, E. M., Kilcoyne, A. L. D., Tyliszczak, T., Weker, J. N., Nishi, Y. & Williams, R. S. Direct Observation of Localized Radial Oxygen Migration in Functioning Tantalum Oxide Memristors. *Advanced Materials* **28**, 2772–2776 (2016).

26. Sowinska, M., Bertaud, T., Walczyk, D., Thiess, S., Schubert, M. A., Lukosius, M., Drube, W., Walczyk, C. & Schroeder, T. Hard x-ray photoelectron spectroscopy study of the electroforming in Ti/HfO_2-based resistive switching structures. *Applied Physics Letters* **100**, 233509 (2012).

27. Kwon, J., Sharma, A. A., Chen, C.-Y., Fantini, A., Jurczak, M., Herzing, A. A., Bain, J. A., Picard, Y. N. & Skowronski, M. Transient Thermometry and High-Resolution Transmission Electron Microscopy Analysis of Filamentary Resistive Switches. *ACS Applied Materials & Interfaces* **8**, 20176–20184 (2016). Publisher: American Chemical Society.

28. Cooper, D., Baeumer, C., Bernier, N., Marchewka, A., Torre, C. L., Dunin-Borkowski, R. E., Menzel, S., Waser, R. & Dittmann, R. Anomalous Resistance Hysteresis in Oxide ReRAM: Oxygen Evolution and Reincorporation Revealed by In Situ TEM. *Advanced Materials* **29**, 1700212 (2017).

29. Chen, J.-Y., Huang, C.-W., Chiu, C.-H., Huang, Y.-T. & Wu, W.-W. Switching Kinetic of VCM-Based Memristor: Evolution and Positioning of Nanofilament. *Advanced Materials* **27**, 5028–5033 (2015).

30. Privitera, S., Bersuker, G., Butcher, B., Kalantarian, A., Lombardo, S., Bongiorno, C., Geer, R., Gilmer, D. C. & Kirsch, P. D. Microscopy study of the conductive filament in HfO_2 resistive switching memory devices. *Microelectronic Engineering* **109**, 75–78 (2013).

31. Yao, J., Zhong, L., Natelson, D. & Tour, J. M. In situ imaging of the conducting filament in a silicon oxide resistive switch. *Scientific Reports* **2**, 242 (2012).

32. Park, G.-S., Kim, Y. B., Park, S. Y., Li, X. S., Heo, S., Lee, M.-J., Chang, M., Kwon, J. H., Kim, M., Chung, U.-I., Dittmann, R., Waser, R. & Kim, K. In situ observation of filamentary conducting channels in an asymmetric Ta_2O_{5-x}/TaO_{2-x} bilayer structure. *Nature Communications* **4** (2013).

33. Kittel, C. *Introduction to Solid State Physics* (Wiley, Hoboken, NJ, 2005), 8th edn.

34. Hubbard, W. A., Kerelsky, A., Jasmin, G., White, E. R., Lodico, J., Mecklenburg, M. & Regan, B. C. Nanofilament Formation and Regeneration During Cu/Al_2O_3 Resistive Memory Switching. *Nano Letters* (2015).

35. Everhart, T. E., Wells, O. C. & Matta, R. K. A novel method of semiconductor device measurements. *Proceedings of the IEEE* **52**, 1642–1647 (1964).

36. Leamy, H. J. Charge collection scanning electron microscopy. *Journal of Applied Physics* **53**, R51–R80 (1982).

37. Hubbard, W. A., Mecklenburg, M., Chan, H. L. & Regan, B. C. STEM Imaging with Beam-Induced Hole and Secondary Electron Currents. *Physical Review Applied* **10**, 044066 (2018).

38. Hubbard, W. A., Lingley, Z., Theiss, J., Sitzman, S., Ayvazian, T., Brodie, M. & Foran, B. Scanning transmission electron microscope mapping of electronic transport in polycrystalline $BaTiO_3$ ceramic capacitors. *Applied Physics Letters* **115**, 133502 (2019).

39. Mecklenburg, M., Hubbard, W. A., Lodico, J. J. & Regan, B. C. Electron beam-induced current imaging with two-angstrom resolution. *Ultramicroscopy* **207**, 112852 (2019).

40. Alam, M. A., Weir, B. E. & Silverman, P. J. A study of soft and hard breakdown - Part I: Analysis of statistical percolation conductance. *IEEE Transactions on Electron Devices* **49**, 232–238 (2002).

41. Houssa, M., Mertens, P., Heyns, M., Jeon, J., Halliyal, A. & Ogle, B. Soft breakdown in very thin Ta_2O_5 gate dielectric layers. *Solid-State Electronics* **44**, 521–525 (2000).

42. Goldsmith, C., Ehmke, J., Malczewski, A., Pillans, B., Eshelman, S., Yao, Z., Brank, J. & Eberly, M. Lifetime characterization of capacitive RF MEMS switches. In *2001 IEEE MTT-S International Microwave Sympsoium Digest (Cat. No.01CH37157)*, vol. 1, 227–230 vol.1 (2001).

43. We refrain from labeling the charge state, aggregation number, or mobility for oxygen vacancies when such information is not provided by our data. Thus, unless otherwise indicated, we do not mean to suggest that the solitary vacancies in Fig. 6 are, for example, either neutral or charged (either before or after electron injection), or single, di-, or tri-vacancies .

44. Bradley, S. R., Bersuker, G. & Shluger, A. L. Modelling of oxygen vacancy aggregates in monoclinic HfO_2 : can they contribute to conductive filament formation? *Journal of Physics: Condensed Matter* **27**, 415401 (2015).

45. Mueller, M. P., Gunkel, F., Hoffmann-Eifert, S. & De Souza, R. A. The importance of singly charged oxygen vacancies for electrical conduction in monoclinic HfO_2. *Journal of Applied Physics* **129**, 025104 (2021).

46. Zhu, W., Ma, T., Zafar, S. & Tamagawa, T. Charge trapping in ultrathin hafnium oxide. *IEEE Electron Device Letters* **23**, 597–599 (2002).

47. Sharma, A. A., Noman, M., Abdelmoula, M., Skowronski, M. & Bain, J. A. Electronic Instabilities Leading to Electroformation of Binary Metal Oxide-based Resistive Switches. *Advanced Functional Materials* **24**, 5522–5529 (2014).

48. Kim, K. M., Choi, B. J., Shin, Y. C., Choi, S. & Hwang, C. S. Anode-interface localized filamentary mechanism in resistive switching of TiO_2 thin films. *Applied Physics Letters* **91**, 012907 (2007).

49. Yoon, J. H., Song, S. J., Yoo, I.-H., Seok, J. Y., Yoon, K. J., Kwon, D. E., Park, T. H. & Hwang, C. S. Highly Uniform, Electroforming-Free, and Self-Rectifying Resistive Memory in the Pt/Ta_2O_5/HfO_{2-x}/TiN Structure. *Advanced Functional Materials* **24**, 5086–5095 (2014).

50. Wu, E. Y. Facts and Myths of Dielectric Breakdown Processes—Part II: Post-Breakdown and Variability. *IEEE Transactions on Electron Devices* **66**, 4535–4545 (2019).

Acknowledgments

The authors acknowledge helpful discussions with Gennadi Bersuker. This work was supported by the UCLA PSEIF, by National Science Foundation (NSF) Science and Technology Center (STC) award DMR-1548924 (STROBE), by NSF awards DMR-1611036 and DMR-2004897, and by the Semiconductor Research Corporation (SRC).

Supplementary Materials for: Imaging Dielectric Breakdown in Valence Change Memory

1. Methods (Figs. S1 – S2)
2. Soft filament formation (Figs. S3 – S7)
3. Additional VCM switching (Figs. S8 – S10)
4. Conduction signatures revealed by STEM imaging (Figs. S11 – S14)
5. Movie captions (Movies S1 – S5)
6. Figures 2–5, as submitted (added in proof)

1 Methods

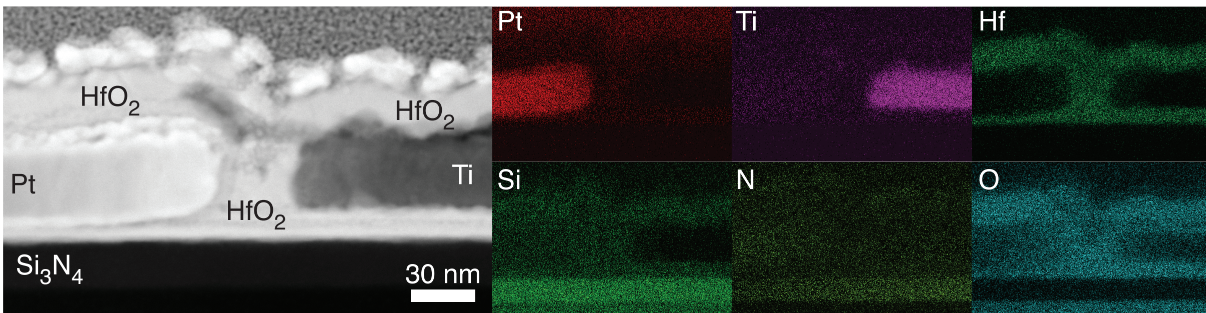

Figure S1: **STEM and EDS images of a cross-sectioned device.** A thin lamella is cut from a slant-vertical Pt/HfO_2/Ti device using a focused Ga ion beam. The materials normally present in a device are labeled in the ADF STEM image on the left. In the cross-section there is SiO_2 below the Si_3N_4, and Au and Pt above the top layer of HfO_2. These materials are present here to facilitate the cross-sectioning process. They are not present in the non-cross-sectioned devices that are the subject of this report.

We fabricate electron-transparent VCM devices on thin Si_3N_4 membranes framed by $200\,\mu$m-thick silicon chips (Figs. 1, S1, S2). Ti/Pt (5/25 nm) leads patterned with optical lithography extend from contact pads at an edge of a mm-scale chip to the edges of the Si_3N_4 membrane window in the center of the chip (*37*). An initial 8-nm thick layer of atomic-layer-deposition (ALD) HfO_2 serves as an adhesion layer for the 30-nm thick Pt bottom electrodes (patterned with electron-beam lithography) that follow. The next 8 nm of ALD HfO_2, the switching layer, is followed by 30-nm thick Ti top electrodes (also patterned via electron-beam lithography) and an 8-nm thick capping layer of ALD HfO_2. This metal-insulator-metal deposition (Pt/HfO_2/Ti) order is the same as that of a standard vertical device, but here the geometry is 'slant-vertical' (*34*). By adjusting the horizontal gap between the Pt and Ti electrodes this architecture can be deformed continuously to allow for good STEM imaging access (positive gap), or to duplicate a commercial device (negative gap, with the electrodes overlapping). The conformal layer

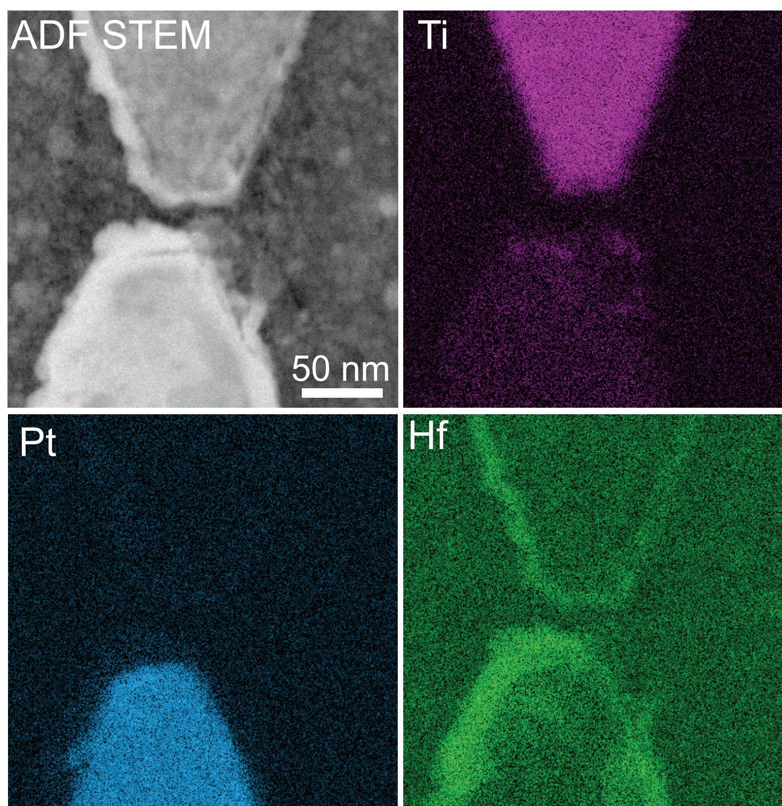

Figure S2: **STEM and EDS images of the Fig. 5 device in plan-view.** These images show a device (and its elemental composition) as it is actually used in the experiments described. The "top" electrode is Ti, and the "bottom" electrode is Pt. The adjectives "top" and "bottom" thus give correct descriptions in two ways: these images are oriented such that the Ti is above the Pt, and the Ti is deposited after the Pt in the device fabrication process. These images also show the ALD HfO_2 to be conformal, as Hf can be seen coating the sidewalls of the electrodes (i.e. the electrodes appear wider in the Hf image than in the Pt or Ti images).

of oxide between the two electrodes ensures that any electrical conduction must penetrate the second HfO_2 layer; no interface connects the two electrodes.

The ALD HfO_2 process uses tetrakis (dimethylamino) hafnium precursor and water as the oxygen source. After each round of ALD, HfO_2 in regions away from switching region is removed with reactive ion etching to allow contact between the optically-defined Ti/Pt leads and the Pt and Ti electrodes that extend over the membrane. The completed, TEM-ready devices feature a protected layer of HfO_2 between the electrodes that is uncompromised by any mechanical polishing or ion milling (Figs. 1, S1, S2).

Electrical transport is measured with a Keithley 6430 sourcemeter, and imaging is performed in an FEI Titan 80-300 TEM in STEM mode. All images are acquired using an 80 kV accelerating voltage to minimize beam damage and promote secondary electron (SE) production. Beam currents are 50 ± 30 pA. STEM EBIC and standard STEM (e.g. BF, ABF, and ADF) images are acquired simultaneously by digitizing in parallel the signal from the transimpedance amplifier (FEMTO DLPCA-200) and the signals from the standard STEM detectors. Typical STEM EBIC images are 256×256 pixels and acquired with a $\sim$100 s frame time.

Figures 4, S9, S10, and S11 show fits to the Poole-Frenkel model for electronic conduction,

$$j = \sigma_0 E \cdot \exp\left(\sqrt{\frac{e^2 E}{\pi\epsilon \cdot k_B^2 T^2}}\right), \tag{1}$$

where $j = I/A$ is the electrical current I per area A, E is the electric field, σ_0 is the zero-field conductivity, $k_B T$ is the thermal energy, and ϵ is the dielectric constant. Taking $E = V/d$ and $R_0 = d/(A\sigma_0)$, we fit the $I(V)$ data with Eq. 1, treating the zero-field resistance R_0 and one of either d, T or ϵ as free parameters. (The form of Eq. 1 prevents the concurrent fitting of more than one of the three parameters d, T and ϵ.) In all cases we fit over the voltage domain indicated by the extent of the red curve.

The magnitude of the power dissipation IV is such that the temperature change due to Joule heating is likely < 1 K. Thus we expect $k_B T$ to have a room-temperature value of 25 meV, d to be about the measured minimum electrode separation, and ϵ to be about $20\epsilon_0 \simeq 1$ e/(V·nm). The fits return d or ϵ about five times the expected value, or T about $\sqrt{5}$ times the expected value, when the other two are fixed at their expected values. Thus this crude implementation (e.g. A, T, E constant along the length of the filament) manages to fit, to within a factor of order unity, the $E \exp[\sqrt{E}]$-dependence characteristic of the Poole-Frenkel model over a broad voltage range using only two adjustable parameters. We conclude that the PF picture of trap-assisted electron transport provides a reasonable explanation of the rate-limiting step in the ON-state electronic conduction through these VCM devices.

2 Soft Filament Formation

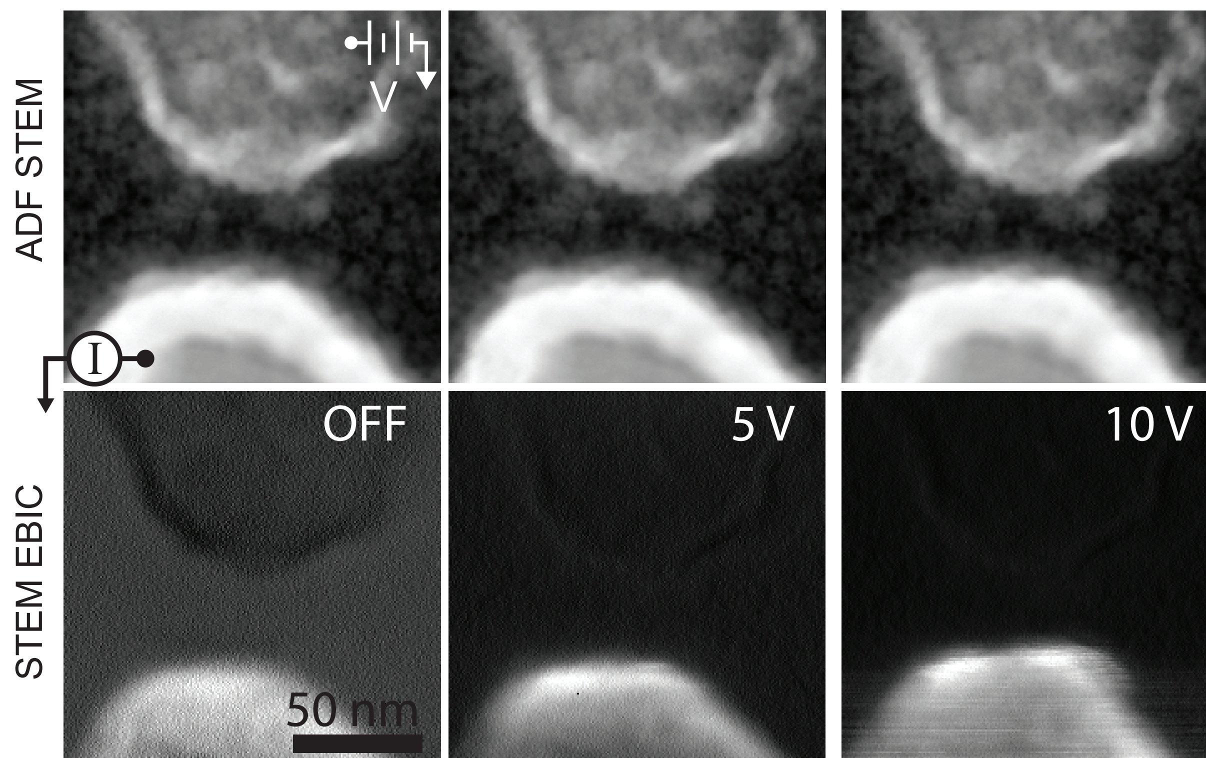

Figure S3: **Soft filament reproducibility.** These data show the device of Figs. 2,4 during a different voltage cycle. The data were acquired after the data of Fig 2, but before the data of Fig. 4. When the positive voltage bias is removed and then reapplied, the soft filament reappears in the same place.

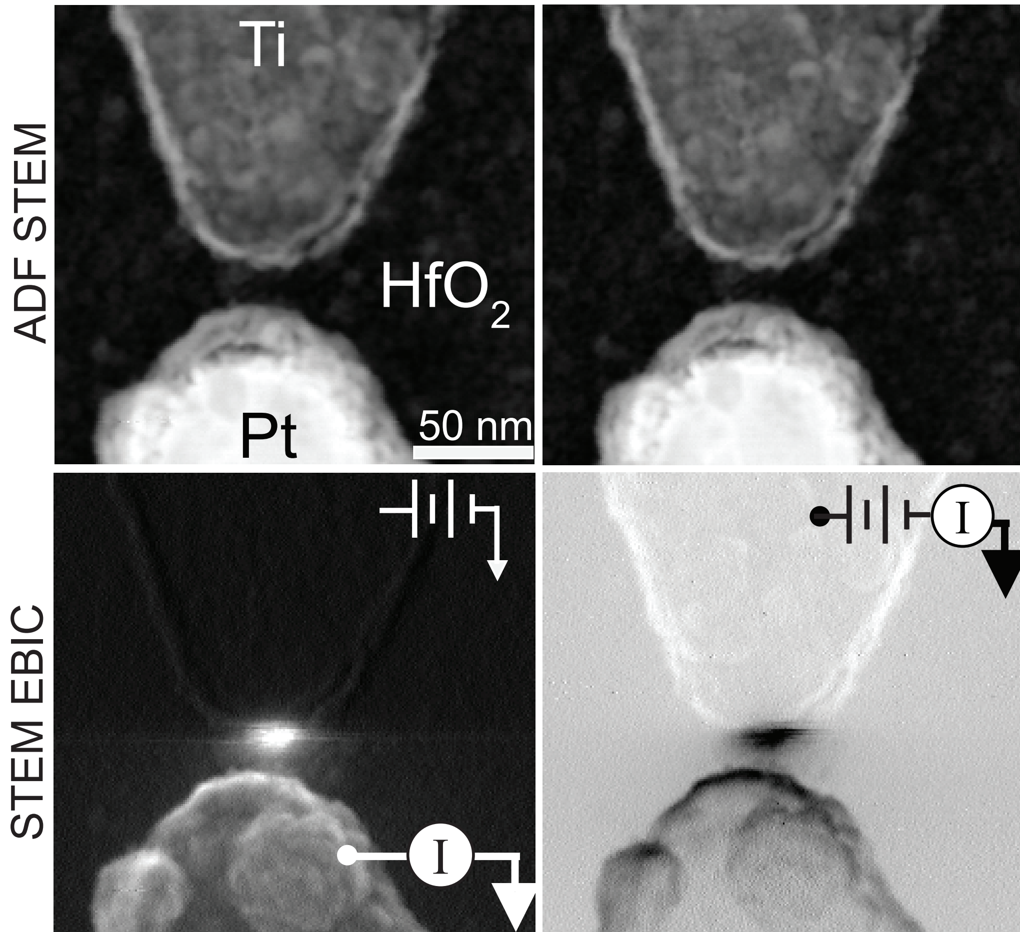

Figure S4: **Choosing to measure the EBIC on the anode, as opposed to the cathode, does not change the conclusions, only the signal-to-noise ratio**. These four images represent two separate acquisitions on the device of Fig. 3. For both acquisitions the Ti is biased to 10 V relative to the Pt. The ADF STEM images (top) show the same view of the device. The STEM EBIC images (bottom), on the other hand, are radically different (Fig. S5) because the preamplifier has been moved. The lower left image (reproduced from Fig. 3) shows the EBIC measured on the Pt. The lower right image shows the EBIC measured on the Ti. At the Ti edge the two EBIC images show equal and opposite EBICs, indicating standard EBIC contrast (i.e. pair separation). Away from the Ti edge the contrast is generated by SEEBIC (i.e. secondary electron emission). In this case the polarity is also reversed, but the magnitudes are unequal (Fig. S5). Not all secondary electrons emitted by one electrode are recaptured by the other, so the signal-to-noise ratio is better on the electrode attached to the TIA. We generally choose to attach the TIA to the cathode, as this arrangement gives the best signal-to-noise ratio for the structures that appear during switching (growing from the cathode).

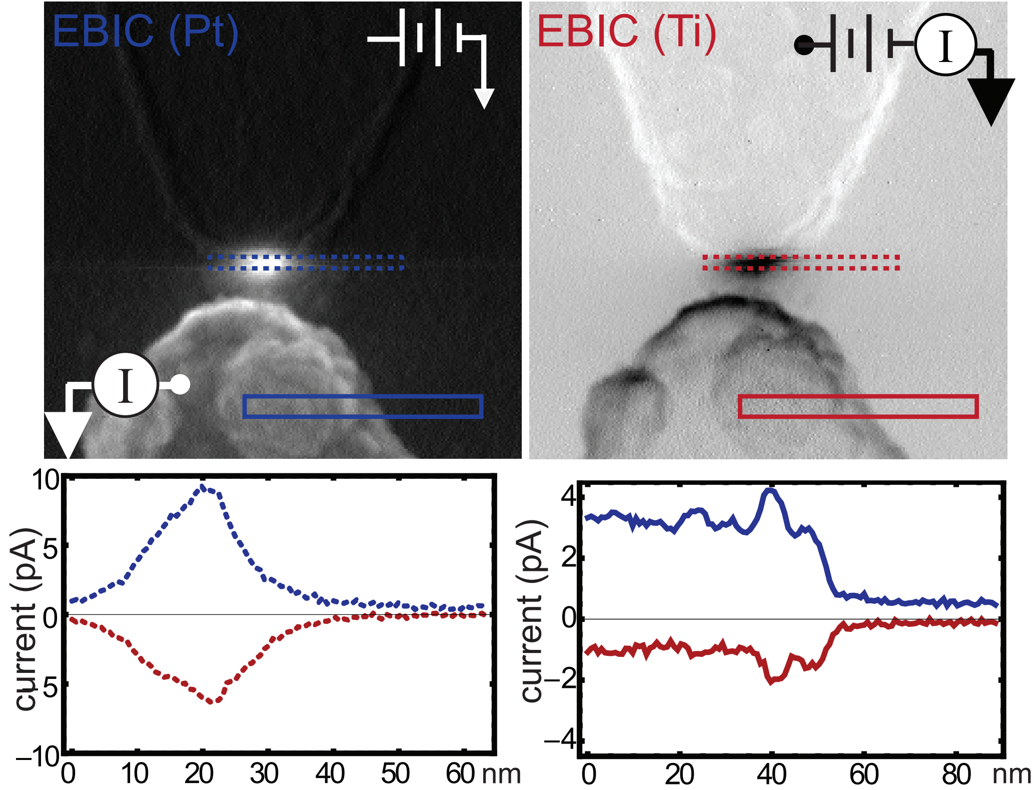

Figure S5: **Comparing the EBICs from two electrodes distinguishes standard EBIC from SEEBIC.** Here each line profile (using the STEM EBIC data from Fig. S4) is acquired from the region indicated by the box outlined with the same color and dashing. Unfortunately, these images are not acquired simultaneously, so this illustration is imperfect. However, at the "intense spot" (dashed boxes) the EBIC is opposite and of approximately equal magnitude in the two EBIC channels, as expected for standard EBIC. Meanwhile, the EBIC produced by the Pt electrode (solid boxes) is $4\times$ larger in magnitude when measured as a hole current from the Pt electrode than when measured as an electron current from the Ti electrode, as expected for SEEBIC.

Very generally, a given EBIC can sometimes be identified as "standard EBIC" or "SEEBIC" based on its size and the material system. Usually standard EBIC is larger than SEEBIC, with the former at times comparable to the beam current and the latter only a few percent of the beam current. Standard EBIC is expected only in regions that have a local electric field, and where it is present it dominates.

In cases where the EBIC mode may be ambiguous or mixed, it can identified quantitatively by measuring the EBIC from two opposing electrodes, ideally simultaneously. In standard EBIC, each hole reaching one electrode has a corresponding electron reaching the other electrode: the EBICs measured at the two electrodes are equal and opposite. In SEEBIC many of the ejected secondary electrons (see "recapture" discussion of Ref. (*37*)) reach ground without passing through a preamplifier. Thus the SEEBIC hole current is larger than the SEEBIC (recaptured) electron current.

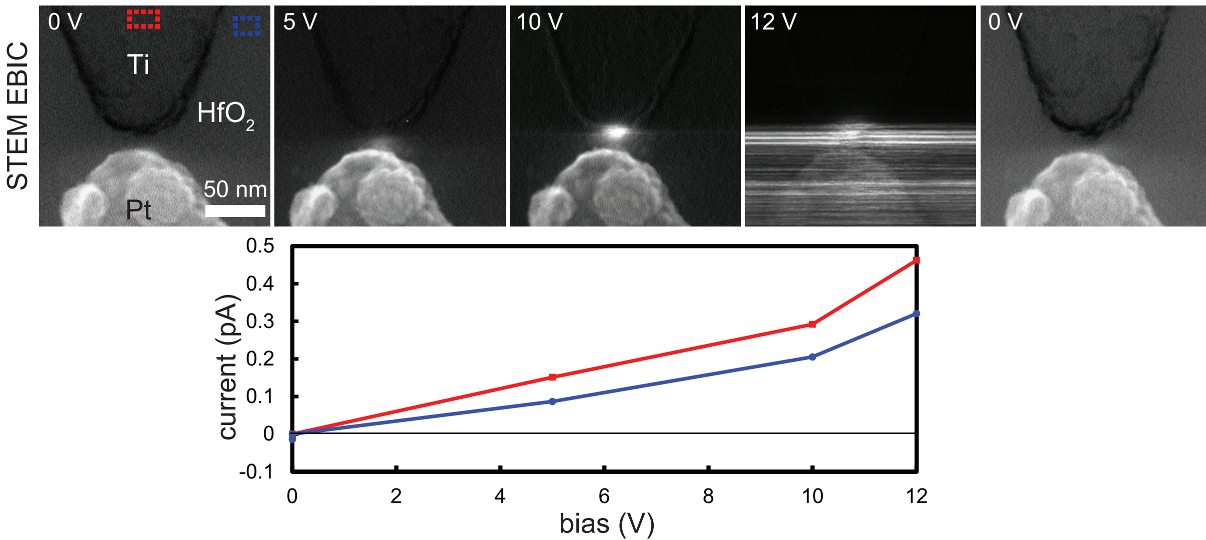

Figure S6: **The device current adds to the EBIC.** As the bias voltage increases, an increasing current that is independent of the imaging electron beam is measured by the TIA. By definition this current is not an EBIC, but it produces an offset, constant at a given voltage, in the EBIC images. We could subtract this small offset, but in this paper we have elected to show the raw data in all line profiles. The streaks in the lower half of the 12 V image indicate that the device is approaching its switching point; the device current is beginning to swamp the EBIC.

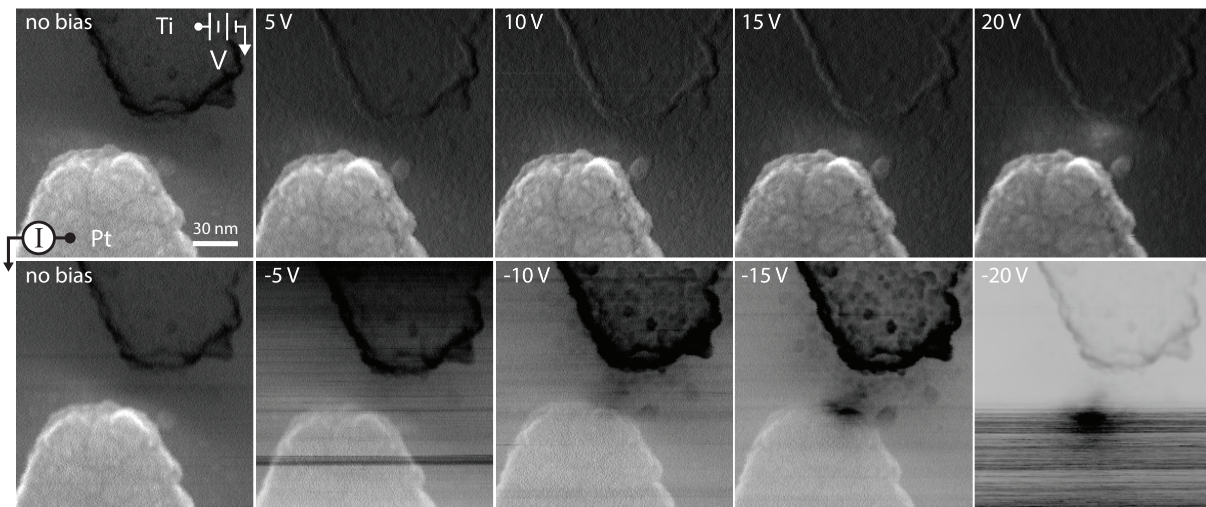

Figure S7: **The soft filament grows from the cathode.** These data show the device of Movie S2. In each STEM EBIC image the current is measured on the Pt electrode and the indicated bias value is applied to the Ti electrode. Under positive bias a bright filament grows “up” from the Ti electrode toward the Pt electrode. Under negative bias a dark filament grows “down” from the Ti electrode toward the Pt electrode. In each case, the magnitude of the current captured from the filament increases as it approaches the opposing electrode. The horizontal streaks in the -20 V image are due to device current and warn of an incipient switch.

3 Additional VCM Switching

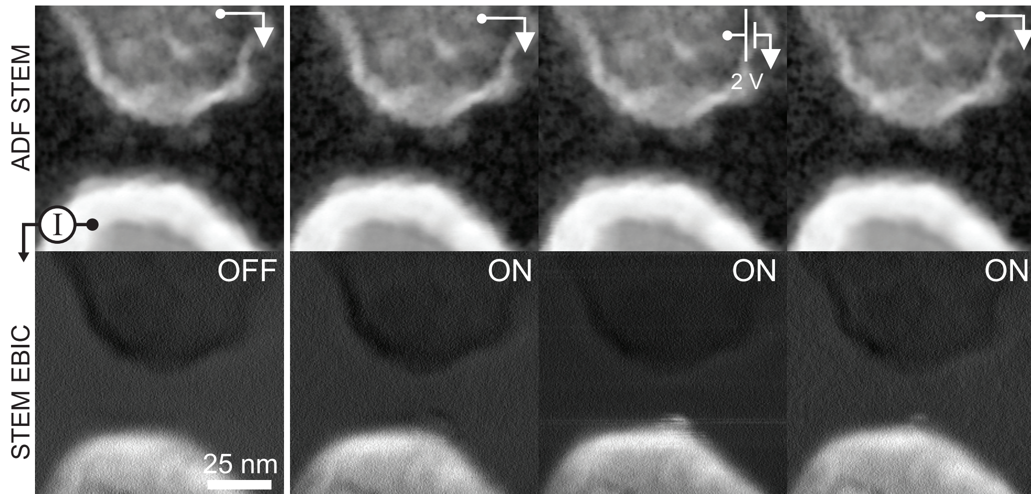

Figure S8: **Hard filament reproducibility.** These STEM ADF and EBIC images show the device of Figs. 2, 4. The leftmost column reproduces the data shown in the rightmost column of Fig. 2 and shows the device in its OFF state. The four columns to the right show the device in a nominal ON state in subsequent cycles not shown in Fig. 4. (The cycle shown in Fig. 4 occurred between the two rightmost shown here. See also Fig. S14.) The indications of the hard filament are particularly subtle in the first of the three ON-states shown. The device is programmed prior to imaging, and direct imaging of the device is avoided to the extent possible while aligning the STEM prior to each image. The EBIC displayed is captured from the Pt (bottom) electrode. The Ti electrode is held at 0 V relative to the Pt in all images except for the second ON-state image, where 2 V were applied to the Ti electrode in a perhaps-successful attempt to mitigate beam-induced changes while imaging. While the device is nominally ON, at 2 V the Poole-Frenkel conduction is small and does not swamp the EBIC.

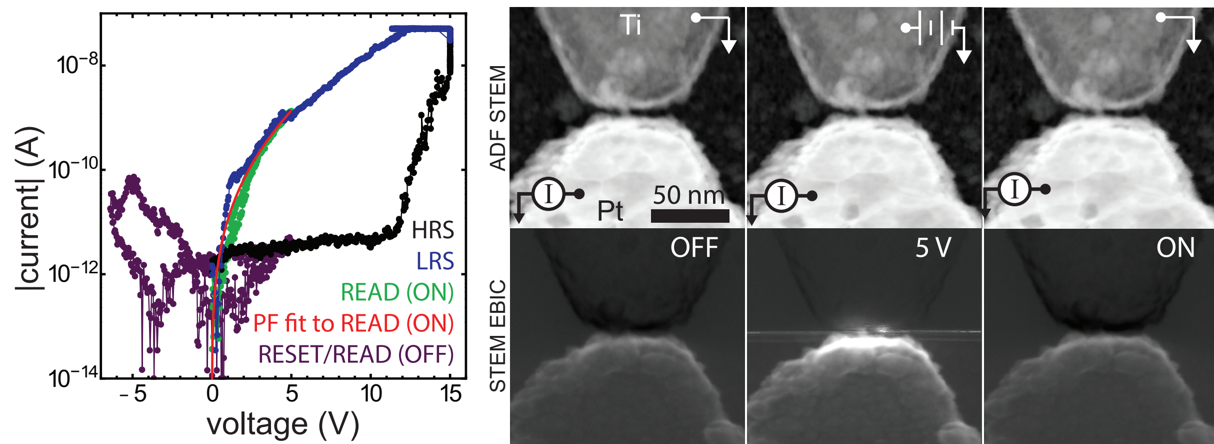

Figure S9: **A small electrode gap changes little but the imaging access.** In this device the apparent separation between the two electrodes is only a few nanometers. However, it shows electrical transport similar to that seen in devices with larger gaps. Standard STEM imaging shows no significant changes as a function of voltage or the device ON/OFF state. At pre-SET voltages STEM EBIC imaging shows bright contrast growing from the Pt electrode (the soft filament) and very bright contrast at the edge of the Ti electrode (large E-fields). In the final STEM EBIC ON-state image, holes generated in the (grounded) Ti electrode always have an easy, direct path to ground; the Ti electrode never charges at all, PF conduction cannot occur, and the Ti electrode appears dark regardless of its ON/OFF state. The small gap prevents us from seeing a hard filament. While the small electrode separation gives relatively poor imaging access, all indications are that physics of the switching process is fundamentally unaltered.

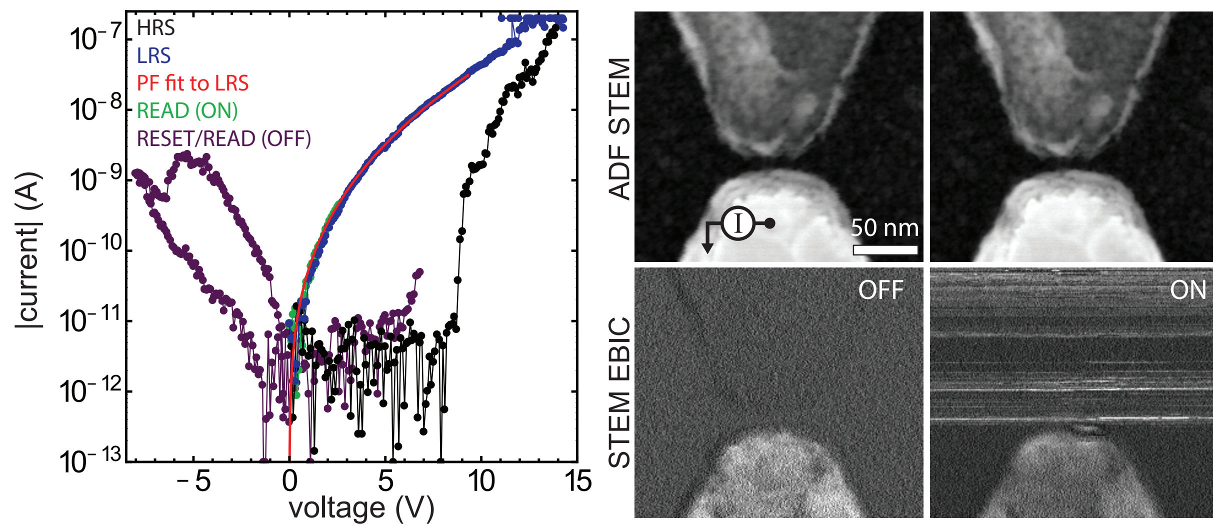

Figure S10: **Signatures of Poole-Frenkel conduction in STEM EBIC images.** These images are acquired after the device has been programmed to the state indicated. In the OFF-state the Ti electrode is grounded (i.e. held at 0 V relative to the Pt). In the ON-state the Ti (top) electrode is floating. As in Fig. 5 (see discussion in Sec. 4), secondary electron emission causes the floating electrode to charge positively, and its intermittent discharges via PF conduction to the Pt (bottom) electrode produce streaking in the image. After the electron beam reaches the gap, the nominally ON-state device is switched OFF, but a hard filament is visible in the gap.

4 Conduction signatures revealed by STEM imaging

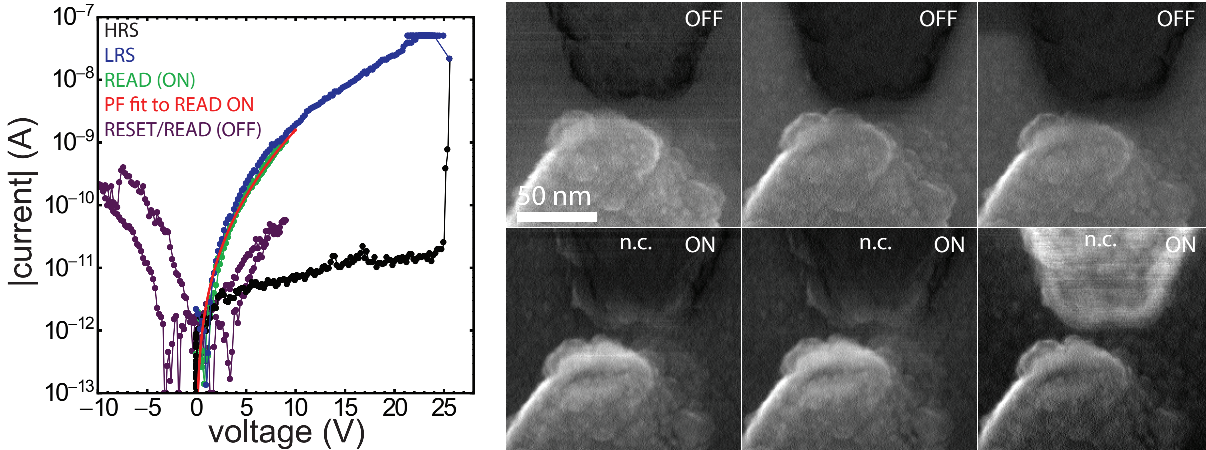

Figure S11: **STEM EBIC imaging reveals the top electrode connections.** This $I - V$ plot shows a typical switching cycle for the device in Fig. 5, and the STEM EBIC images (all the images here are STEM EBIC) show the same device in its OFF and ON states. In all images the EBIC is measured on the lower, Pt electrode, and no bias is applied to the device while the image is acquired. In the upper row of images the Ti is grounded and in the lower row the Ti is floating. After being switched OFF (upper row), the Ti (top) electrode appears dark; when the STEM beam hits the Ti, some SE are recaptured by the Pt, and the holes left behind have an easy route to ground. After being switched into a nominal ON state (lower row), the appearance of the Ti electrode varies. With no particular care taken, the electrode appears somewhat dark (lower row, first two images); exposure to the beam during alignment and focusing has turned the nominally ON device OFF. However, applying a voltage of 9 V to the Ti electrode until immediately before imaging preserves the ON state. Observing this protocol (lower row, rightmost image, and Fig. 5) shows a bright Ti electrode; the Ti is PF-connected to the Pt — more beam-induced holes than electrons are making it to the TIA, and intermittent charging is producing streaks in the image.

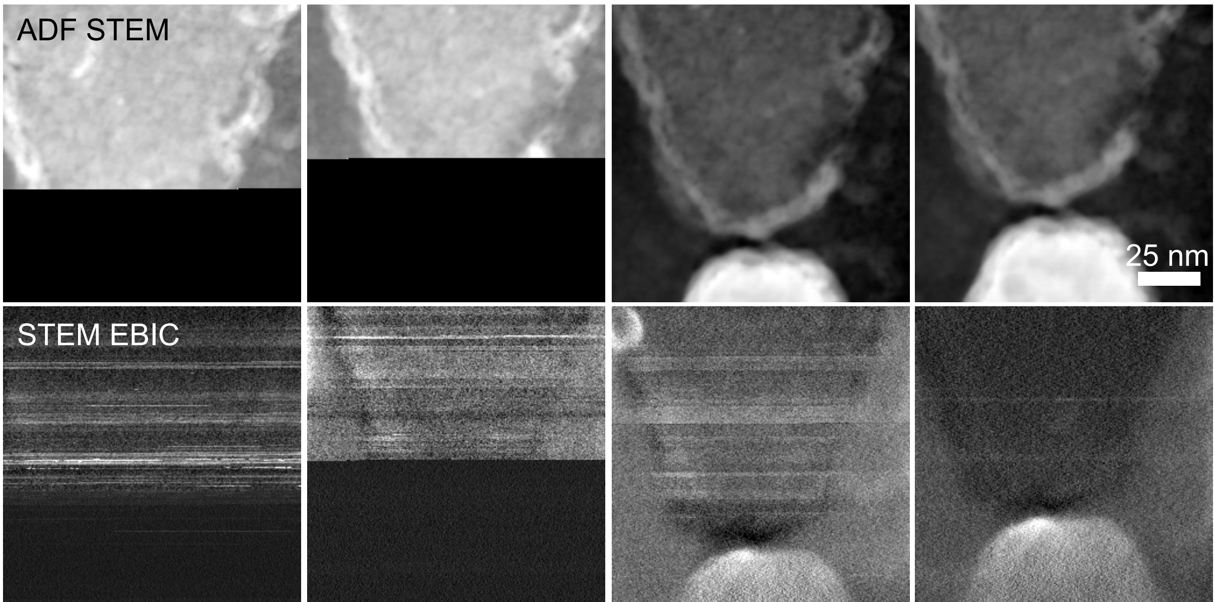

Figure S12: **Exposing the filament specifically (as opposed to the whole device) to the electron beam produces a RESET.** These images, some of them partial, are shown in their order of acquisition from left to right. The device is SET before the first image, the TIA is connected to the Pt electrode and the Ti electrode is floating. In the first two images the STEM acquisition is interrupted before the rastering beam reaches the gap. Both images show streaking on the Ti electrode, indicating intermittent PF discharges: the device is still in the ON state. For the third image the acquisition is allowed to run to completion, and streaking is evident on the Ti electrode. However, the subsequent (fourth) image shows no streaking on the Ti. Evidently, when the beam rastered across the gap during the third image it switched the nominally ON-state device into its OFF state.

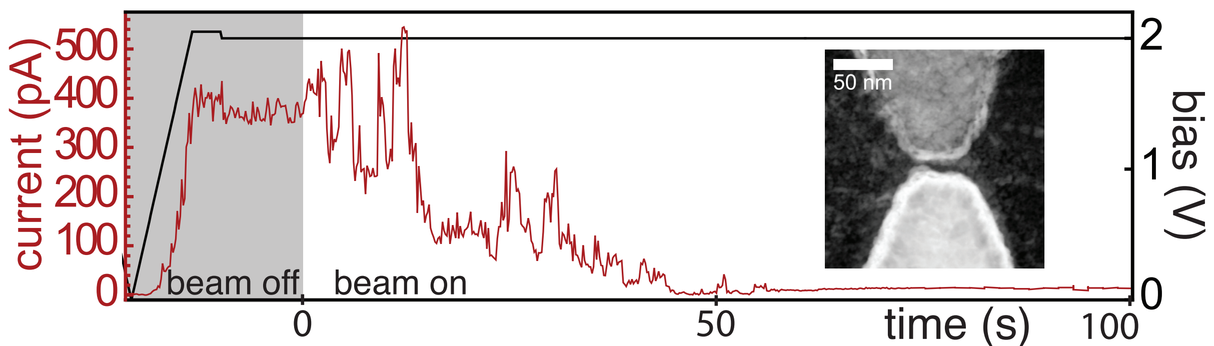

Figure S13: **Electron beam exposure turns an ON-state device OFF.** The device, shown in the ADF STEM inset, was SET with the beam blanked. Then 2 V were applied to the upper Ti electrode relative to the lower Pt electrode, and the device current was monitored as the device was imaged repeatedly with a 2 s frame time. The device current generally decreases with beam exposure, dropping to near zero after ∼55 s of imaging, much shorter than the typical STEM EBIC frame time of ∼100 s.

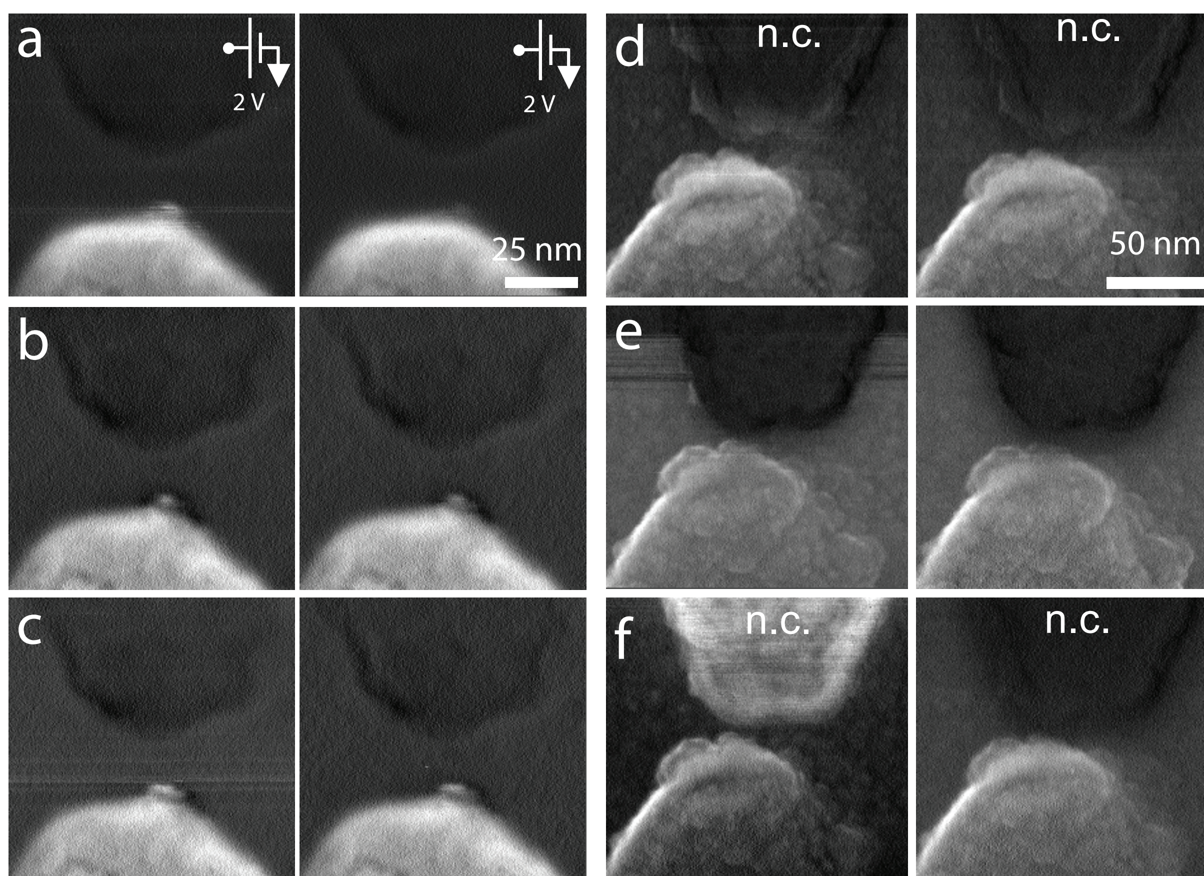

Figure S14: **The hard filament is robust to STEM beam exposure.** Parts (a)–(c) show the device of Figs. 2, 4, and parts (d)–(f) show the device of Fig. 5. These STEM EBIC images consist of pairs acquired in direct succession, with the right image of each pair acquired immediately after the left image. While the hard filament (region of bright EBIC near the Pt edge) may dim in the second image, it does not disappear. In all images the EBIC is measured on the lower, Pt electrode. Unless otherwise indicated as floating (n.c. for no connection) or biased, the Ti electrode is grounded.

5 Supplementary Movies

Included with this report are 5 movies showing VCM devices as visualized by standard STEM and STEM EBIC imaging. (Bright field (BF), annular bright-field (ABF), and annular dark-field (ADF) STEM are all examples of standard STEM.) Apart from some distortions created by sample drift, the applied voltage, and perhaps change of focus, BF, ABF, and ADF STEM imaging show no significant changes to the VCM devices as a function of the applied bias. STEM EBIC imaging, on the other hand, shows the region electrically connected to the Pt electrode growing toward the Ti as the soft filament develops. Captions specific to the individual movies follow:

- **Movie S1: Soft filament in the Figs. 2, 4 device (BF STEM, ADF STEM, and STEM EBIC imaging).** Here biases varying from 0–17.5 V and then back to 0 V are applied to the Ti (top) electrode relative to the Pt (bottom) electrode. At biases ≤ 10 V the EBIC image contrast is generated by SEEBIC. At biases ≥ 15 V the device is almost ON, and intermittent device current produces streaking over the Pt electrode in the EBIC image. The last frame shows that the voltage-induced changes are volatile: the device returns to its initial state when the bias returns to 0 V.
- **Movie S2: Soft filament and large E-field in the Fig. S7 device (BF STEM, ADF STEM, and STEM EBIC imaging).** Here biases varying from 0–20 V are applied to the Ti (top) electrode relative to the Pt (bottom) electrode. At biases ≤ 16 V the EBIC image contrast is generated by SEEBIC. At biases $\gtrsim 18$ V the large E-field at the tip of the soft filament creates standard EBIC contrast that intensifies with increasing voltage.
- **Movie S3: Soft filament and large E-field in the Fig. 3 device (BF STEM, ADF STEM, and STEM EBIC imaging).** Here biases varying from 0–12 V and then back to 0 V are applied to the Ti (top) electrode relative to the Pt (bottom) electrode. At biases ≤ 5 V the EBIC image contrast is generated by SEEBIC. At 10 V the large E-field at the tip of the soft filament creates strong standard EBIC contrast. At the highest bias, 12 V, the device is almost ON and intermittent device current produces streaking over the Pt electrode in the EBIC image. The last frame shows that all of these bias-induced changes are volatile: when the bias returns to 0 V, the device returns to its initial state.
- **Movie S4: Soft filament and large E-field in a device with a fabrication defect (BF STEM, ABF STEM, ADF STEM, and STEM EBIC imaging).** Here biases varying from 0–12.5 V are applied to the Ti (top) electrode relative to the Pt (bottom) electrode. This device has a point that, because of the device geometry, looks particularly vulnerable to DB. At biases $\lesssim 8$ V the EBIC image contrast is generated by SEEBIC. At biases ≥ 9 V the large E-field at the tip of the soft filament creates standard EBIC contrast that intensifies with increasing voltage. At biases ≥ 12 V the device is almost ON and intermittent device current produces streaking in the EBIC image, especially when the STEM beam is rastering through the gap between the electrodes.
- **Movie S5: Soft filament and large E-field in another device (BF STEM, ABF STEM, ADF STEM, and STEM EBIC imaging).** Here biases varying from 0–15.5 V and then back to 0 V are applied to the Ti (top) electrode relative to the Pt (bottom) electrode. At biases $\lesssim 11$ V the EBIC image contrast is generated by SEEBIC. At biases ≥ 12 V the large E-field at the tip of the soft filament creates standard EBIC contrast that intensifies with increasing voltage. At biases ≥ 13 V the device is almost ON and intermittent device current produces streaking in the EBIC image, especially when the STEM beam is rastering through the region with the large E-field.

6 Figures 2–5, added in proof

As submitted to the journal, Figs. 2–5 show actual imaging data. This faithful representation does not survive the production process, so the as-submitted figures are reproduced here.

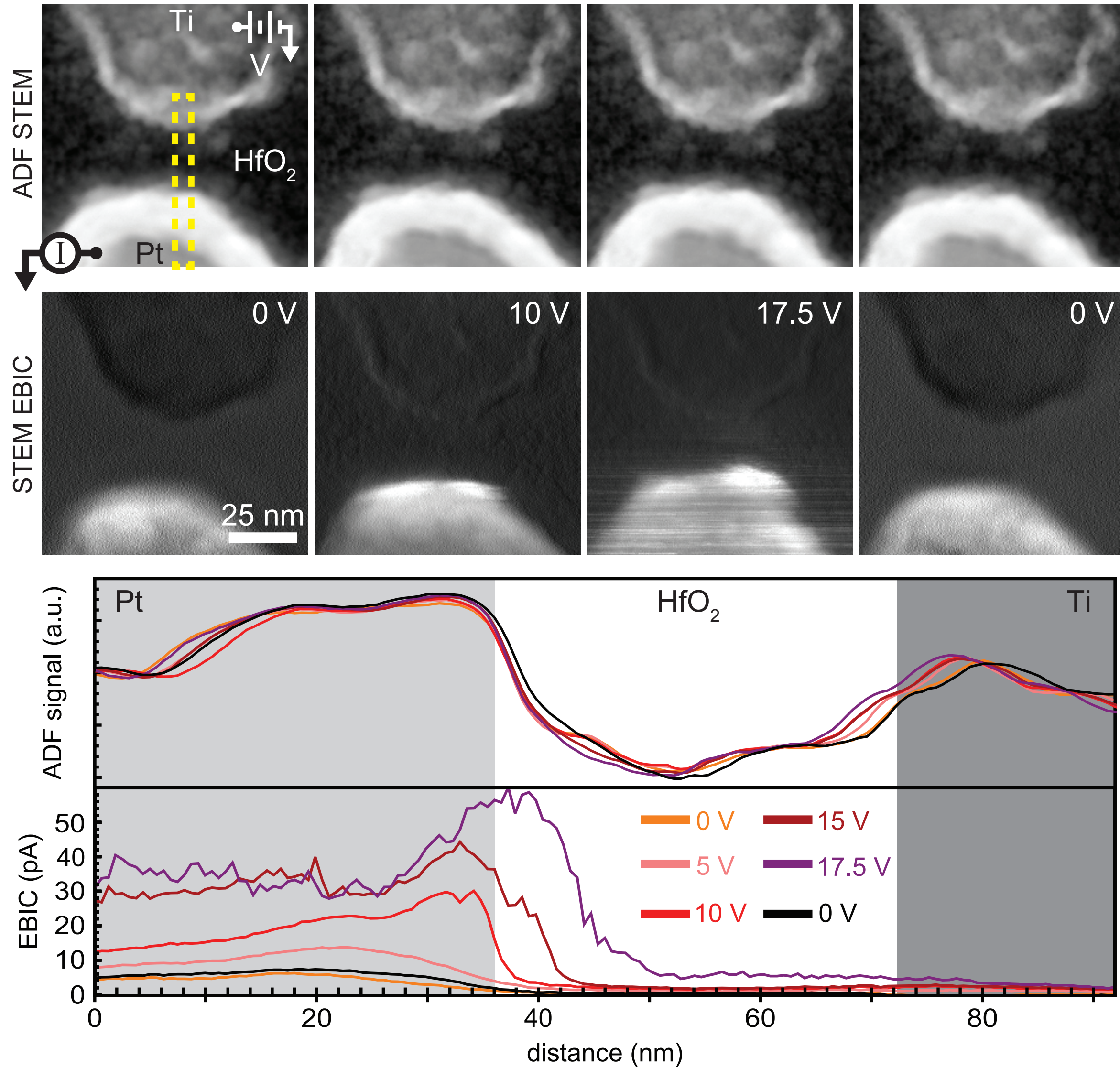

Figure S15: **Soft filament formation and dissolution, reproduction of Fig. 2.** (top row) STEM ADF images of a slant-vertical Pt/HfO_2/Ti VCM device show no changes as the Ti–Pt bias voltage is increased. (second row) Simultaneously acquired STEM EBIC images, on the other hand, show the region electrically connected to the Pt expanding into the gap. See also Movie S1. (bottom) Line profiles extracted by averaging over the rectangular region indicated in the first ADF image show these trends quantitatively (including additional bias values from images not shown). Symbols in the first ADF image indicate the electrical connections for applying the bias and measuring the EBIC.

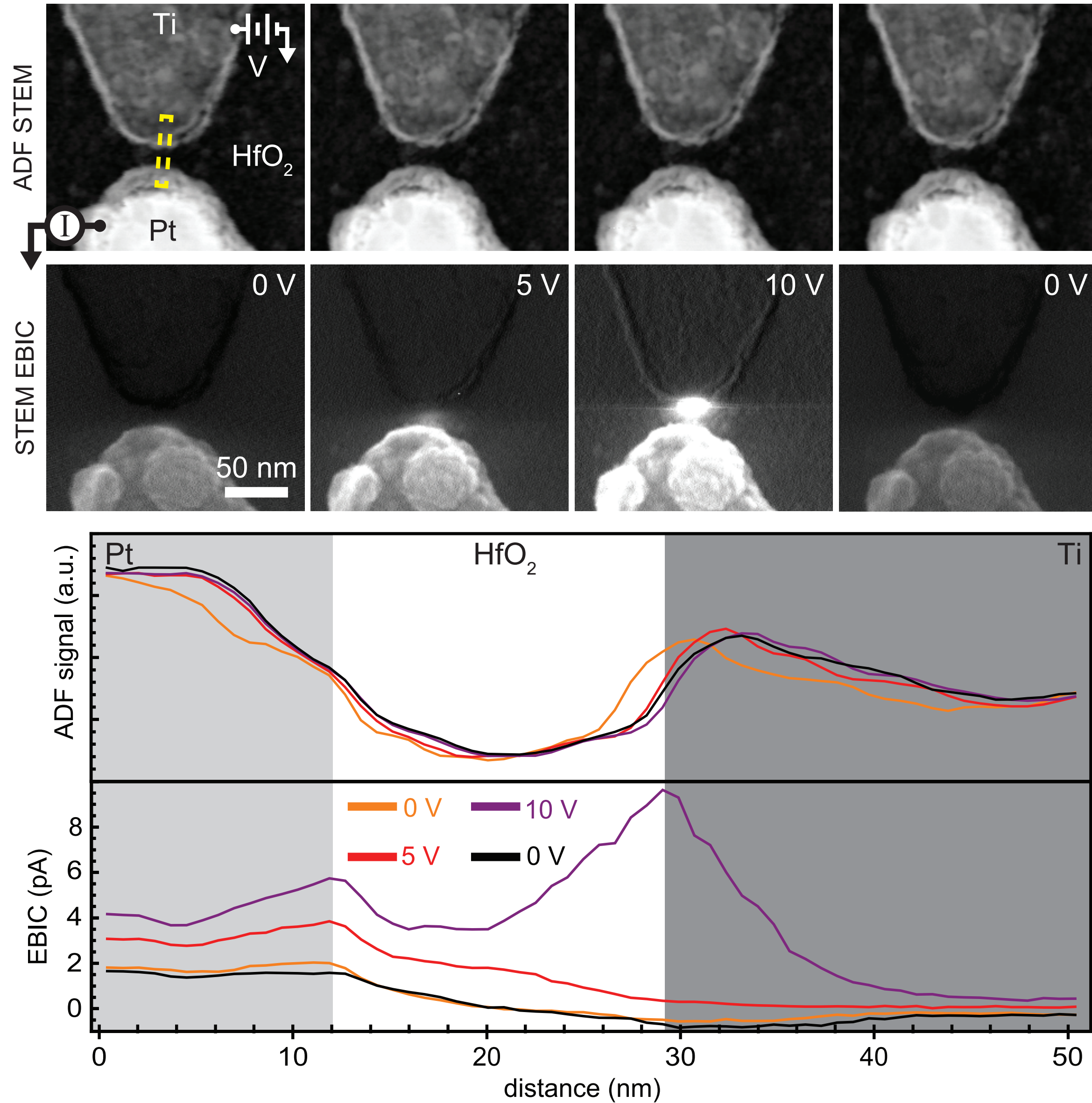

Figure S16: **Large E-field at the switching point, reproduction of Fig. 3.** (top) STEM ADF imaging shows no changes as a Ti/HfO_2/Pt device is biased at 0 V, 5 V, and 10 V, and 0 V. (second row) EBIC imaging shows a soft filament grow, almost connect, and then disappear. See also Movie S3. (bottom) Line profiles of the ADF and EBIC signals from the dashed yellow region indicated in the 0 V ADF image show the corresponding contrast values quantitatively. At non-zero bias, small device currents (e.g. 300 fA at 10 V) add to the EBIC (Fig. S6).

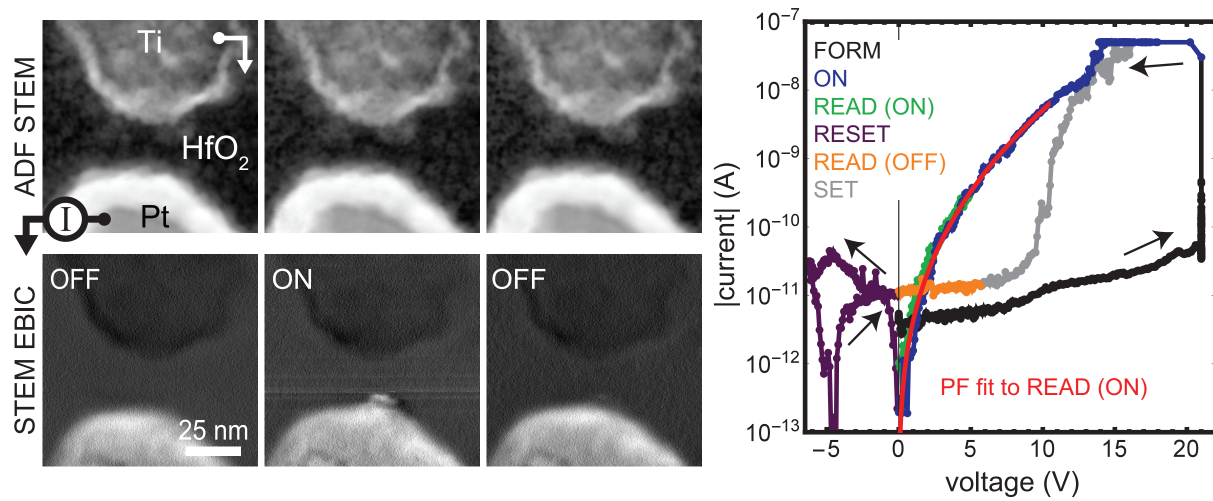

Figure S17: **Hard filament formation and dissolution, reproduction of Fig. 4.** ADF imaging (left, top row) shows no changes between the ON and OFF states of the VCM device of Fig. 2. STEM EBIC imaging (left, bottom row), however, again shows obvious changes between the ON and OFF states, with the most marked being a sharp protuberance at the Pt electrode's apex. Each image is acquired after voltage programming (see text), but with a 0 V bias. The $I - V$ plot (right) shows a complete cycle of this device. The LRS data is well fit by the PF model (red curve). The apparent "battery" (i.e. current $I \neq 0$ at voltage $V = 0$ and vice versa) in the HRS is an artifact of stray capacitance, the large device resistance, and the voltage ramp rate $dV/dt = 0.3$ V/s. Note that, because of device currents and beam sensitivity, STEM EBIC images cannot be directly associated with all points on the plot.

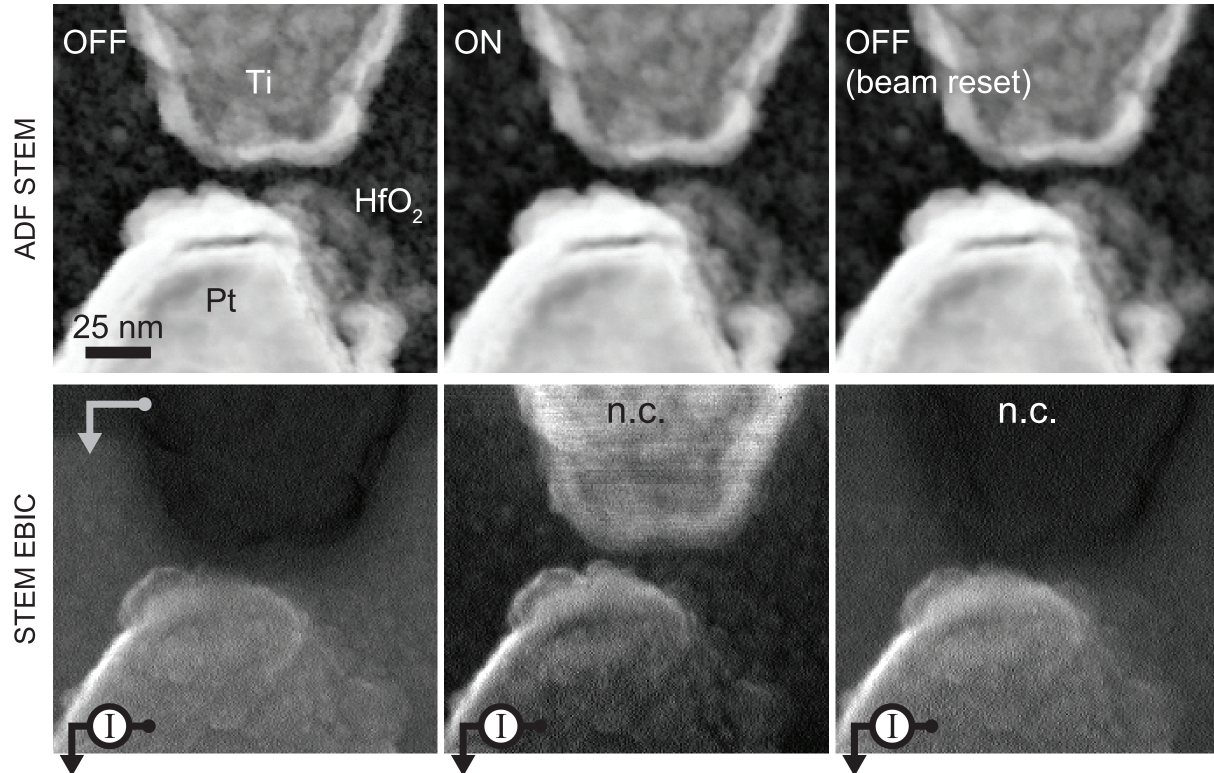

Figure S18: **ON-state conduction switched OFF by STEM beam, reproduction of Fig. 5.** Images acquired directly after a -10 V device RESET (left column) show negative EBIC from the Ti electrode, indicating that the device is OFF. With the beam blanked, the device is then SET and held at 9 V until immediately before another image acquisition (center column). The intermittent positive EBIC from the Ti electrode in this state indicates a non-ohmic connection to the Pt electrode. A final image (right column) immediately following shows only negative EBIC from the Ti electrode, indicating that the device has been RESET by the beam. ADF imaging (top row) shows no sign of these state changes, which are only made evident with EBIC imaging (bottom row). A ‘n.c.’ label on the Ti electrode indicates ‘no external connection’.